

Ryerson University  
Faculty of Engineering and Architectural Science  
Department of Aerospace Engineering

# Aerodynamic Optimization of the Von Karman Nose Cone for a Supersonic Sounding Rocket

**Taruansh Singh Qaumi**

AER870  
Undergraduate Thesis  
Faculty Advisor - Dr. Paul Walsh  
16/04/2021



## **Abstract**

Nose cone design is very much reliant on the conditions of the rocket's flight path. The design is dependant on the altitude, velocity profile, materials, and other factors. This report will look at optimizing a rocket nose cone design based on preliminary measurements, aerodynamic factors, and engineering design process. This analysis will be done utilizing ANSYS Fluent to conduct CFD on 2D symmetric Von Karman nose cones of varying fineness ratios.



## Acknowledgements

The Author would like to thank Dr. Walsh for his consultation and support on this project. The feedback and support provided was invaluable which helped to push this project to achieve its results. The Author would also like to thank Ryerson University and the Department of Aerospace Engineering for providing this opportunity to work on an Undergraduate Thesis project. Furthermore, the Author would like to thank Ryerson Rocketry Club for providing the flight data.



# Contents

|   |             |
|---|-------------|
| List of Figures   | v           |
| List of Tables  | vi          |
| <b>1 Introduction</b>                                     | <b>1</b>    |
| <b>2 Literature Review</b>                                | <b>2</b>    |
| 2.1 Nose Cone Geometries . . . . .                        | 2           |
| 2.2 Comparison Studies . . . . .                          | 3           |
| <b>3 Design</b>   | <b>5</b>    |
| 3.1 Initial Assumptions and Conditions . . . . .          | 5           |
| 3.2 Parameters . . . . .                                  | 6           |
| 3.3 Nose Cone Geometry . . . . .                          | 6           |
| 3.4 Optimization Method . . . . .                         | 7           |
| 3.5 Pairwise Comparison Chart . . . . .                   | 7           |
| <b>4 Setup</b>  | <b>9</b>    |
| 4.1 Computational Domain . . . . .                        | 9           |
| 4.2 Meshing . . . . .                                     | 10          |
| 4.3 Fluent Settings . . . . .                             | 13          |
| <b>5 Validation</b>                                       | <b>15</b>   |
| 5.1 Comparison Tests . . . . .                            | 15          |
| 5.2 Y+ Values . . . . .                                   | 16          |
| 5.3 Mesh Independence Study . . . . .                     | 16          |
| <b>6 Analysis</b>   | <b>19</b>   |
| 6.1 Observations . . . . .                                | 19          |
| 6.2 Optimized Nose Cone Selection . . . . .               | 26          |
| 6.3 Next Steps . . . . .                                  | 32          |
| <b>7 Conclusion</b>                                       | <b>33</b>   |
| <b>8 References</b>                                       | <b>34</b>   |
| <b>A Results.m</b>  | <b>i</b>    |
| <b>B Von-Karman-Profile-Coordinates.m</b>                 | <b>iv</b>   |
| <b>C Fluent Settings</b>                                  | <b>v</b>    |
| <b>D Computation Domain Construction and Mesh Process</b> | <b>xiii</b> |

|          |   |            |
|----------|---|------------|
| <b>E</b> | <b>GCI Calculations</b>                   | <b>xiv</b> |
| E.1      | Grid Refinement Factor . . . . .          | xiv        |
| E.2      | Critical Variables . . . . .              | xiv        |
| E.3      | Apparent Order . . . . .                  | xiv        |
| E.4      | Extrapolated Critical Variables . . . . . | xiv        |
| E.5      | Approximated Relative Error . . . . .     | xiv        |
| E.6      | Extrapolated Relative Error . . . . .     | xiv        |
| E.7      | Grid Convergence Index . . . . .          | xv         |
| <b>F</b> | <b>Tabulated Results</b>                  | <b>xvi</b> |

## List of Figures

|      |   |      |
|------|---|------|
| 2.1  | Qualitative Drag Comparison. . . . .                            | 3    |
| 3.1  | Velocity Profile of the Rocket. . . . .                         | 5    |
| 3.2  | Initial Von Karman Geometry. . . . .                            | 7    |
| 4.1  | Computational Domain. . . . .                                   | 10   |
| 4.2  | Split Face Geometry For Meshing. . . . .                        | 11   |
| 4.3  | Nose Cone Mesh. . . . .   | 12   |
| 4.4  | Mesh Granularity. . . . .                                       | 12   |
| 4.5  | Boundary Layer and Meshing at Nose Cone Apex. . . . .           | 13   |
| 4.6  | Boundary Conditions. . . . .                                    | 14   |
| 5.1  | Validation Case Computational Domain. . . . .                   | 15   |
| 5.2  | $y^+$ Plot for FR 7 at Mach 2.5. . . . .                        | 16   |
| 6.1  | All Tested Von Karman Geometries. . . . .                       | 19   |
| 6.2  | Coefficient of Drag Vs Mach Number First Iteration. . . . .     | 20   |
| 6.3  | Drag Vs Mach Number First Iteration. . . . .                    | 21   |
| 6.4  | Drag Coefficient Vs Mach Number Second Iteration. . . . .       | 22   |
| 6.5  | Drag Vs Mach Number Second Iteration. . . . .                   | 23   |
| 6.6  | Drag Coefficient Vs Mach Number Third Iteration. . . . .        | 24   |
| 6.7  | Drag Vs Mach Number Third Iteration. . . . .                    | 25   |
| 6.8  | Drag Breakdown. . . . .   | 26   |
| 6.9  | Drag Coefficient Vs Fineness Ratio (Mach 1.1 - Mach 3). . . . . | 27   |
| 6.10 | Drag Coefficient Vs Fineness Ratio (Mach 0.3 - Mach 1). . . . . | 28   |
| 6.11 | Drag Vs Fineness Ratio (Mach 1.1 - Mach 3). . . . .             | 29   |
| 6.12 | Drag Vs Fineness Ratio (Mach 0.3 - Mach 1). . . . .             | 30   |
| 6.13 | Static Temperature at Mach 2.5. . . . .                         | 31   |
| C.1  | Fluent General Settings. . . . .                                | v    |
| C.2  | Fluent Viscous Model. . . . .                                   | vi   |
| C.3  | Fluent Material Properties. . . . .                             | vii  |
| C.4  | Fluent Material Properties Sutherland's Law. . . . .            | vii  |
| C.5  | Fluent Cell Zone Conditions. . . . .                            | viii |
| C.6  | Fluent Boundary Conditions. . . . .                             | ix   |
| C.7  | Fluent Reference Values. . . . .                                | x    |
| C.8  | Fluent Courant Number. . . . .                                  | xi   |
| C.9  | Fluent Initialization. . . . .                                  | xii  |

## List of Tables

|    |   |      |
|----|---|------|
| 1  | Atmospheric Conditions. . . . .                       | 6    |
| 2  | Initial Nose Cone Parameters. . . . .                 | 6    |
| 3  | Pairwise Comparison Chart. . . . .                    | 7    |
| 4  | Mesh Statistics . . . . .                             | 17   |
| 5  | Critical Variables. . . . .                           | 17   |
| 6  | Apparent Order and Extrapolated $C_d$ Values. . . . . | 17   |
| 7  | Approximate Relative Error. . . . .                   | 18   |
| 8  | Extrapolated Relative Error. . . . .                  | 18   |
| 9  | Fine and Course Grid Convergence Index. . . . .       | 18   |
| 10 | Mass Criterion. . . . .                               | 31   |
| A1 | $C_D$ Values for FR 5.25, 6, 6.5. . . . .             | xvi  |
| A2 | $C_D$ Values for FR 5.25, 6, 6.5. . . . .             | xvi  |
| A3 | Drag Values for FR 5.25, 6, 6.5. . . . .              | xvii |
| A4 | Drag Values for FR 6.75, 7, 8. . . . .                | xvii |

## Nomenclature

|                   |   |
|-------------------|---|
| $\theta$          | Curvature Angle   |
| $AOA$             | Angle of Attack   |
| $C$               | Haack Variable  |
| $C_D$             | Coefficient of drag, dimensionless parameter  |
| $CFD$             | Computational Fluid Dynamics  |
| $D$               | Nose Cone Diameter  |
| $deg$             | Shorthand for Degrees   |
| $E$               | Young's Modulus   |
| $e_a^{i,i-1}$     | Approximate Relative Error  |
| $e_{ext}^{i,i-1}$ | Extrapolated Relative Error   |
| $Eq.$             | Shorthand for Equation  |
| $Fig.$            | Shorthand for Figure  |
| $Fluent$          | Analytical software produced by ANSYS   |
| $FR$              | Fineness Ratio  |
| $GCI$             | Grid Convergence Index  |
| $h$               | Grid Size   |
| $I$               | Area Moment of Inertia  |
| $L$               | Nose Cone Length  |
| $M$               | Mach Number   |
| $N$               | Elements  |
| $O$               | Nodes   |
| $p$               | Apparent Order  |
| $P_{cr}$          | Buckling Load   |
| $R$               | Nose Cone Radius  |
| $r$               | Grid Refinement Factor  |
| $Re$              | Reynolds' Number  |
| $SATP$            | Standard Ambient Temperature and Pressure   |
| $y+$              | dimensionless quantity; measures distance from the wall in terms of viscous lengths |

# 1 Introduction

The purpose of this report is to provide an optimized nose cone design for a given velocity profile and diameter. Utilizing the velocity profile provided by the Ryerson Rocketry team and additional parameters such as the current dimensions of the nose cone. These parameters will such as the length and diameter of the nose cone which will serve as an initial starting point for the optimization. This report does not look at material properties or stress analysis, instead it focuses on analysing the aerodynamic properties to find an optimal design. Specifically the the drag force and coefficient of the rocket nose cone were calculated at various points in the velocity profile. Additionally, included in the report is the setup used in ANSYS Fluent to conduct the analysis.

## 2 Literature Review

### 2.1 Nose Cone Geometries

A variety of nose cone geometries can be utilized for the rocket depending on the flight conditions and other factors. The three main groups of nose cone geometries are conical, ogival, and 'power-series'/hemispherical. Each of these categories has specific effects on the drag performance, thermal properties, and the structural integrity of the nose cone. The general dimensions which are used to size the nose cone shape are R and L. R is the radius of the nose cone base, and L is the length of the nose cone. The 2D profile of the nose cone is laid out on a x-y plane and the profile is revolved around the center line (c/l). The x-axis coordinates vary from 0 to L and the y coordinates vary from 0 to R. [3]

The conical shape is the most basic geometry used for nose cone design. The conical nose cone shape is common and easy to manufacture as compared to other geometries. It also provides an aerodynamic design with low drag values. The next is the ogival nose cone geometry. This nose configuration is used more frequently than conical geometries. This is due to several advantages ogival geometries have such as greater volume for given length and radius, increased structural integrity due to blunted nose, and slightly lower drag. Finally, the last shape category is the hemispherical/'power series' geometries which are used on missiles. They are used especially on use IF (infrared) seeker missiles. These subset of nose cone geometries offer more volume and greater structural integrity than other nose cone subsets. This advantage is however countered by a steep increase in drag, as the wave drag may be 6-7 times that of an ogive. [2]

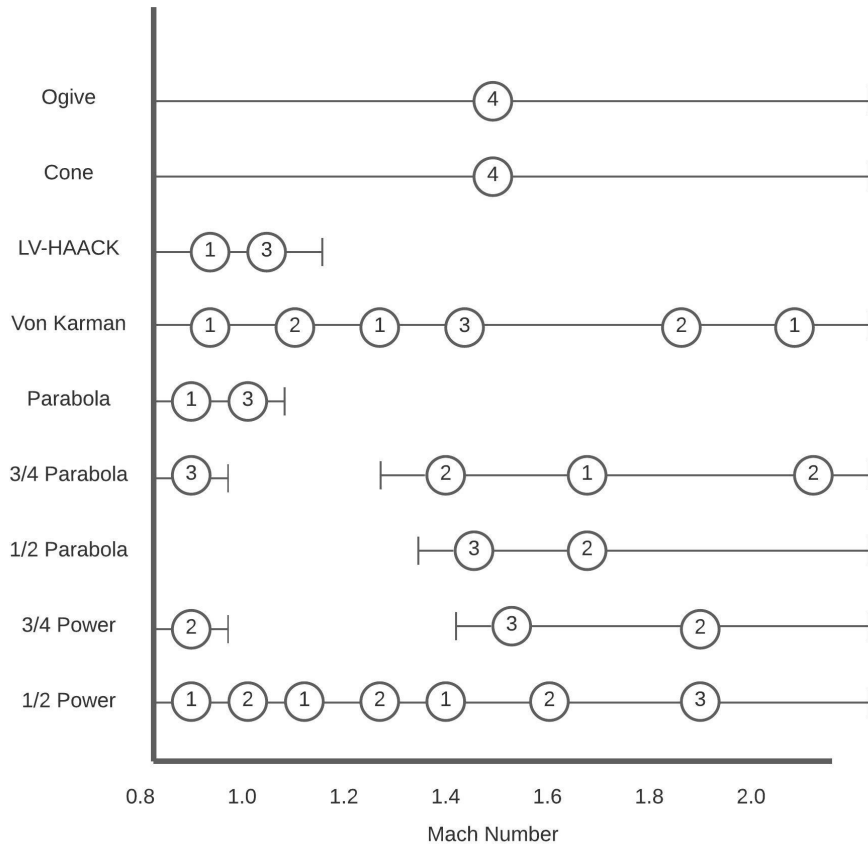


Figure 2.1: Qualitative Drag Comparison.

The figure above is a recreation of the qualitative drag comparison provided in the text, *Missile Configuration Design*. The text was written by S.S.Chin, the chief aerodynamics engineer at the Martin Company (now Lockheed Martin). Considering that the sounding rocket will spend much of its time flying between Mach 2 and 3, the above chart recommends the Von Karman geometry as the best option.

## 2.2 Comparison Studies

There have been various studies which looked at the performance of different nose cone geometries. In a CFD drag analysis conducted by Lucas Carvalho and Geovanio Filho compared the drag performance of four main nose cone geometries: conic, tangent ogive, parabolic, and elliptical. Their results showed that the use of conic nose cones resulted in higher drag in subsonic regions when compared to the other nose cone geometries. The other nose cone geometries

were similar in terms of performance with the no specific geometries proving to be the best.

In Girish Kumar and Dr. Pravin V Honguntikar's paper a similar analysis was conducted on the performance of nose cone geometries, this time in transonic flow. Once again it was shown that the conic profile was outperformed by the other geometries in terms of the drag performance. This paper also reported that the ogive nose cone geometry generated the least amount of drag when compared to conic and blunt nose cone geometries. In general, the results of these studies have supported the relations shown in figure 2.1.

In addition to drag performance, the referenced studies looked at the temperature and pressure gradients of the nose cone geometries both in subsonic and supersonic regions. The results agreed that the thermal properties of conic nose cone profiles were higher than other geometries. Another study by Ashish Narayan et al conducted an analysis on the effects of hypersonic flow across nose cone geometries. The study also looked at the varying the fineness ratio of the nose cone geometry and its effects on the heat flux and total drag. The results showed that at a given velocity as the fineness ratio is increased the resulting total drag values decreased. Some of the studies were conducted in 2D while others were done in 3D. Based on the findings of these studies and the additional information provided above the ogive nose cone geometry seems to be the best choice. Given that the rocket velocity will range up to Mach 3, the Von Karman geometry is selected as the candidate for optimization. [1][4][5][6]

### 3 Design

#### 3.1 Initial Assumptions and Conditions

As was previously mentioned in section ?? the nose cone is being optimized for a specific velocity profile. The image below represents the velocity profile for the rocket as provided by the Ryerson Rocketry Club (RRC). As shown below the rocket nose cone will be flying through speeds up to Mach 3. The velocity range was broken down into three regions: subsonic (Mach 0.3-0.8), transonic (Mach 0.8-1.2), and supersonic (Mach 1.2-3). As displayed in figure 3.1, the rocket spent minimum time in the subsonic region, therefore the starting Mach speed was chosen Mach 0.3.

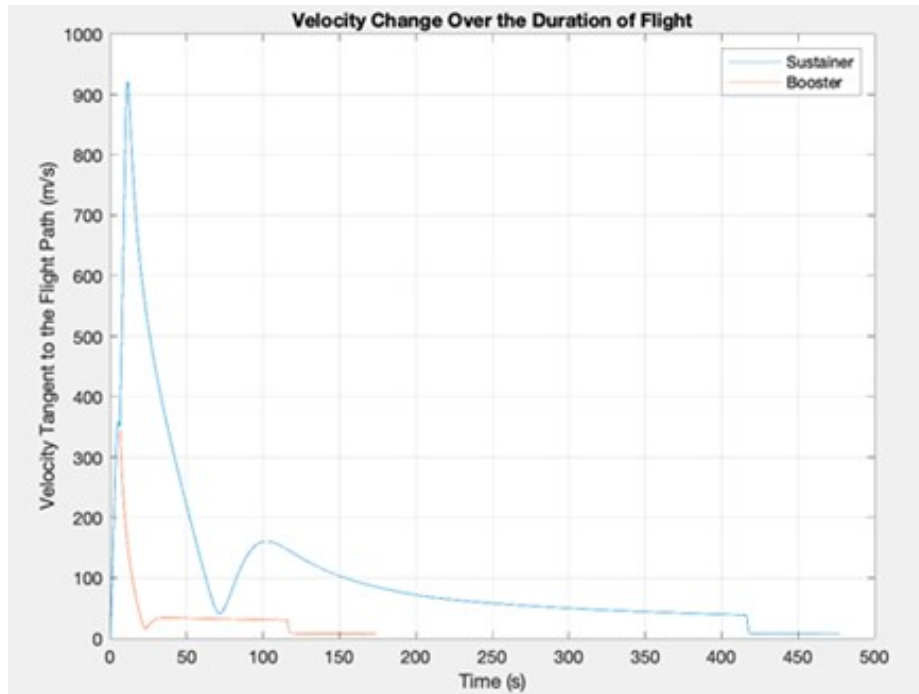


Figure 3.1: Velocity Profile of the Rocket.

While the rocket is expected to reach an altitude of 90,000 ft and undergo various changes to pressure, temperature, and other variables, a few assumptions were made to simplify the simulations conducted. The first assumption is that the nose cone simulations will take place within a wind tunnel at sea level conditions as presented in table 1 below. Secondly it is assumed, there will be no changes in the free-stream temperature, pressure, or any other variables. All simulations for all nose cone geometries will be conducted in the same manner and environment. Thirdly it is assumed that the nose cone will be at a zero AOA with the oncoming wind.

Table 1: Atmospheric Conditions.

| Parameter   | Value                        |
|-------------|------------------------------|
| Pressure    | 101.325 kPa                  |
| Temperature | 300 K                        |
| Density     | 1.18 kg/m <sup>3</sup>       |
| Viscosity   | 8.90 × 10 <sup>-4</sup> Pa·s |

### 3.2 Parameters

Based on the information collected from both the reference material and studies the nose cone geometry selected was the Von Karman nose cone. As stated in the conditions above, the diameter of the nose cone geometry is fixed. The only variables that varied were the fineness ratio and length. The starting parameters of the design and their values are provided in the table 2 below. These parameters were based on previous year's design and served as the initial values for the optimization process.

Table 2: Initial Nose Cone Parameters.

| Parameter              | Value             |
|------------------------|-------------------|
| Diameter               | 5.15in            |
| Radius                 | 2.575in           |
| Initial Length         | 27in              |
| Initial Fineness Ratio | Von Karman Series |

### 3.3 Nose Cone Geometry

The Von Karman nose cone geometry is a subset of the Haack series of nose cone geometries. Below equations 3.1 and 3.2 describe the Haack series of nose cone geometries with the variable C representing the different variations of the nose cone. There are two main values for C that have significance. The first is C=1/3 which indicates minimum drag for a given length and volume, it is represented as LV-Haack. The second is C=0 which indicated minimum drag for a given length and volume, it is represented as LD-Haack. [3]

$$\theta = \arccos\left(1 - \frac{2x}{L}\right) \quad (3.1)$$

$$y = \frac{R}{\sqrt{\pi}} \sqrt{\theta - \frac{\sin 2\theta}{2} + C \sin \theta^3} \quad (3.2)$$

Using the above equations, the initial Von Karman nose cone is shown plotted below in figure 3.2.

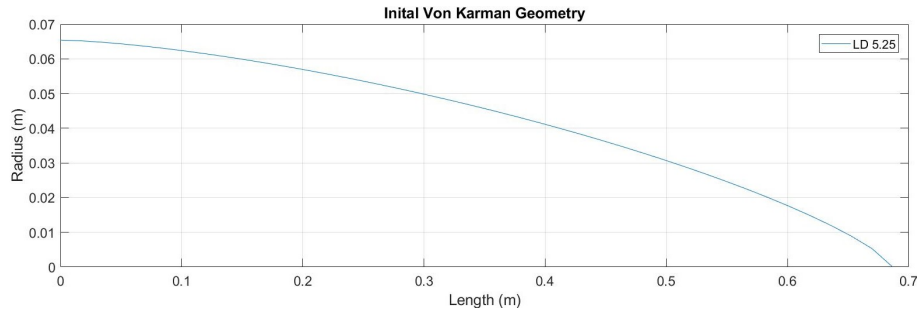


Figure 3.2: Initial Von Karman Geometry.

### 3.4 Optimization Method

The main goal of the optimization was to find the fineness ratio and therefore the dimensions which resulted in minimum drag. As mentioned in the section 3.2 the only variables changed were the fineness ratio (FR), specifically the length until an optimal nose cone geometry was found. A few other criteria were added in as well such as the mass, thermal properties, and structural integrity of the nose cone. The process would begin by choosing three additional fineness ratios. As evidenced by the literature review increasing the fineness ratio results in a decrease of drag whereas decreasing the ratio leads to the opposite. Along with the initial input of the fineness ratio based on the reference geometry, three other values were chosen. Each of these fineness ratios were then run through the predicted flight velocity profile. The drag coefficients and force values from ANSYS Fluent simulations were then be plotted against the Mach numbers. The plotted data was then reviewed for two possible outcomes. If it seemed that the drag values were consistently dropping with increasing fineness ratios, then the additional criteria would be utilized to provide a stopping criterion. If, however the values plotted were approaching a limit or turning point an emulation of the Bisection method in conjunction with other criteria would be used to help provide a stopping point.

### 3.5 Pairwise Comparison Chart

The pairwise comparison chart below discusses the details for the additional criteria. The table also provides the weightings assigned to each of the metrics.

Table 3: Pairwise Comparison Chart.

| Goals                |   | A   | B   | C   | D   | Score | Weights |
|----------------------|---|-----|-----|-----|-----|-------|---------|
| Drag                 | A | *** | A   | A   | A   | 4     | 40%     |
| Mass                 | B | -   | *** | B   | B   | 3     | 30%     |
| Thermal Properties   | C | -   | -   | *** | C   | 2     | 20%     |
| Structural Integrity | D | -   | -   | -   | *** | 1     | 10%     |

(Note: “\*\*\*” counts as 1 point)

Based on the pairwise comparison chart above the most important metric for the design was the drag with it having 40% of the weight in the design criteria. This is justified as the Cd value and therefore the drag force is the most important aspect of the nose cone in terms of achieving a higher apogee. Additionally, less drag also mean less stress on the rest of the rocket structure.

The second most important criteria was the mass of the nose cone geometry. This criterion has a major impact on the aerostructure of the rocket and overall performance. While it is important to reduce the drag there will be a limit after which there are diminishing returns. Therefore, by assigning the second most importance to the mass with a weighting of 30% it helps to provide a stopping point for the optimization.

The final two criteria are thermal properties and structural integrity. These two criteria take third and fourth place in terms of their weightings. Thermal properties and structural integrity while being important factors are weighted at 20% and 10% respectively. The Von Karman nose cone geometry being a subset of ogive nose cones, it already has better thermal properties and structural integrity due to their blunted nose.

## 4 Setup

As stated in section 3.4 above the simulations for each nose cone geometry will be conducted in Ansys Fluent. The following sections will go through the setup requirements for the simulations, such as computational domain, meshing, and Fluent settings.

### 4.1 Computational Domain

The first step of the setup was the computational domain. There were two computational domains which were dominantly used in the reference literature, the rectangular domain and bullet shaped domain. Initially the rectangular geometry was used to create the computational domain. This however proved difficult when meshing since the meshing was leading to a high element count in regions of little importance as well as low mesh quality. The second option, the bullet shaped computational domain was far easier to mesh and complimented the curvature of the nose cone profile, leading to better mesh quality. The final computation domain can be seen in figure 4.1 below. Since the nose cone angle of attack was consistently zero, the domain was halved and made axisymmetric. Additionally, with the nose cone attached to the rocket, the domain was cut right at the end of the nose cone and the outlet was placed there.

The computational domain was sketched in CATIA's generative shape design. As seen in figure 4.1 below lines 1 and 2 laid out the initial shape of the domain. The top of the domain was a line with length  $L$  which connected lines 3 and 2. Lines 3 and 1 were connected using an oval which is represented as line 4. Initially the vertical distance between the nose cone and the top of the domain was  $9.7 D$ , but after initial simulations showed the shockwaves reflecting, the distance was increased.

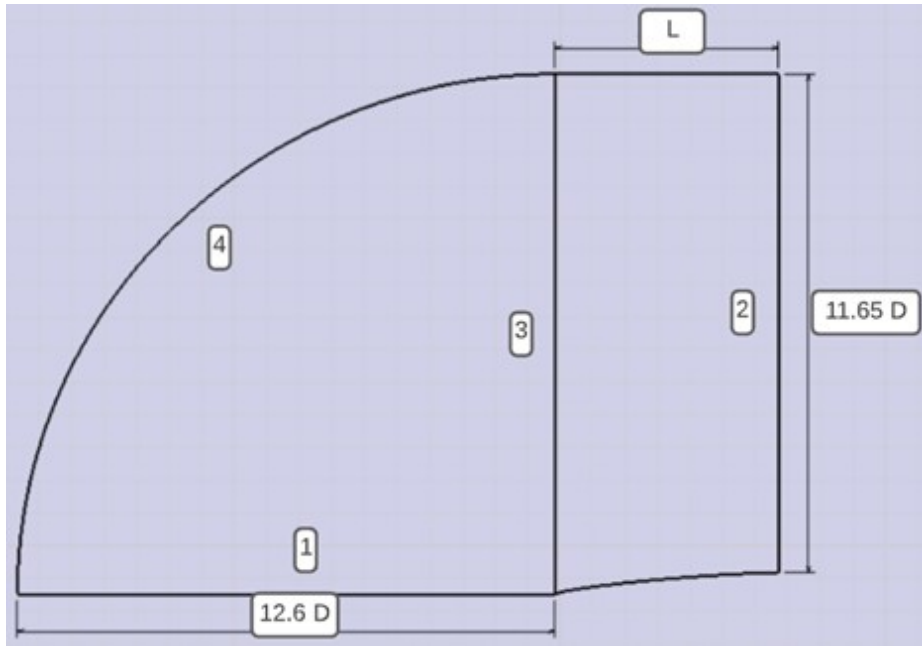


Figure 4.1: Computational Domain.

## 4.2 Meshing

The meshing process for the computational domain was an iterative process. When the mesh was being iterated on there were two main goals that had to be accomplished. The first goal was to ensure the important features of simulation, such as the shockwaves, boundary layer, etc. were captured. The second goal was to ensure the mesh allowed smooth transition of the flow to avoid numerical errors. The second goal was hampered since the pandemic restricted access to more processing power; therefore, the element count was kept within reasonable limits. To achieve these goals the geometry of the computational domain was split into various faces and helped to provide a more gradual mesh. These splits were based on a few iterations where different cuts were tested to see how the mesh developed and what improvements needed to be made. The final mesh was created using a combination of a structured and unstructured elements.



Figure 4.2: Split Face Geometry For Meshing.

In figure 4.2 the splits in the geometry can be seen. Faces 1 and 2 contained structured elements, this helped to lessen the computing resources needed in relatively phenomenon free zones. The rest of the faces numbering 3-8 were made up of the unstructured mesh. These areas being closer to the nose cone profile, were meshed more densely to capture all important flow behaviours. Each of the pairs such as faces 3 and 4 were meshed representing a level of the mesh. As the elements would get closer to the nose cone profile, they would cross the levels and get finer. It was ensured that while the elements were getting finer, the transitions would be gradual to decrease the amount of numerical errors that would be encountered.

The figure below represents the finest mesh that was created through the grid convergence study. It was also the meshed that was utilized for all simulation runs.

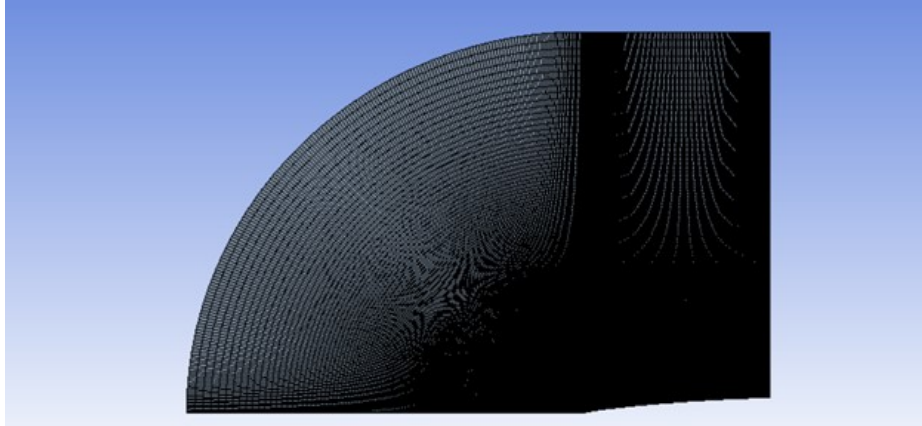


Figure 4.3: Nose Cone Mesh.

In Fig. 4.4 below depicts the gradual levels through which mesh granularity was increased.

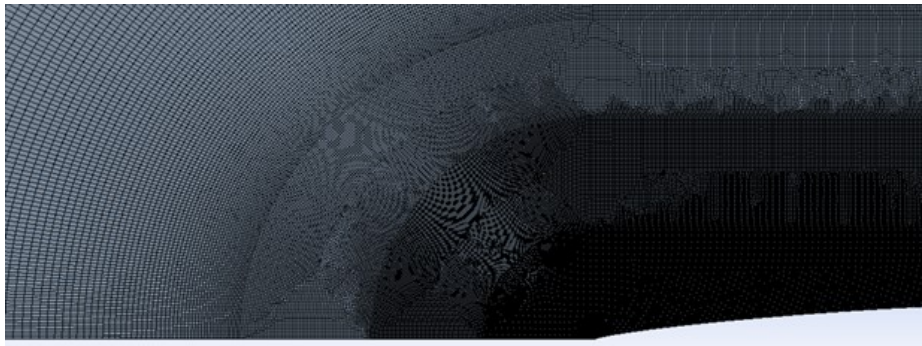


Figure 4.4: Mesh Granularity.

The final figure below displays the inflation layer which represented the boundary layer. Additionally, a sphere of influence was added to the apex of the nose cone profile to increase the local mesh quality and helped to predict the flow more accurately at the nose. Additional information concerning the mesh generation and the exact setting can be found within section ?? of the Appendix.

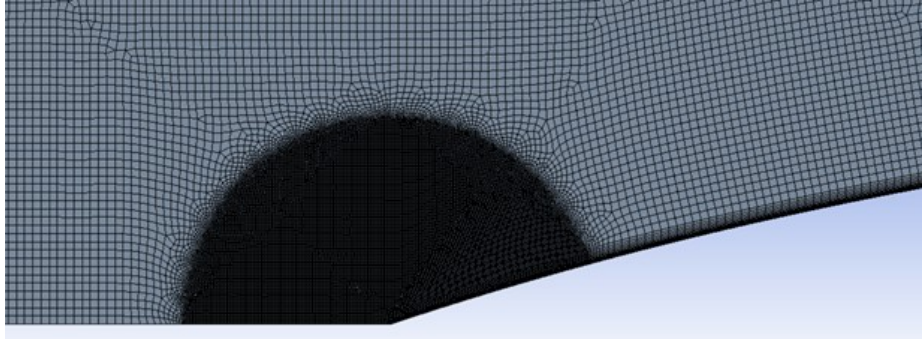


Figure 4.5: Boundary Layer and Meshing at Nose Cone Apex.

### 4.3 Fluent Settings

Once the meshing was completed the next step was to conduct the simulations using Fluent's watertight workflow. The setting for Fluent's workflow can be broken down into a few tasks. The first set of tasks were to setup the general settings. Since the starting Mach number was 0.3 the density-based solver was chosen to account for the compressibility effects. The planar space was set to axisymmetric since the computational domain was halved. The other general settings were left at their default setting. The second set of tasks were setting up the material properties. With the flow being compressible it was important to change the density and viscosity of the fluid, in this case air. The density was set to an ideal gas, and the viscosity was set to Sutherland's Law (3 coefficient method). Both these settings make the density and viscosity dependant on temperature which is required for compressible flow.

The final set of tasks were setting the viscous solver and the boundary conditions. The viscous solver chosen was the Spalart-Allmaras model. The main reasoning for choosing this model as opposed to the default k- model was computational resources. The Spalart-Allmaras model is a relatively simple one-equation model that solves a modeled transport equation for the kinematic eddy (turbulent) viscosity. Additionally, the model was designed specifically for aerospace applications involving wall-bounded flows. The model has been shown to provide good results for boundary layers subjected to adverse pressure gradients. There are downsides to the model such as under-predicting separation however since the computational domain cuts off at the end of the nose cone separation is not modeled. The model along with being resource conservative is also forgiving in terms of meshing therefore making it a great choice given low computational resources.

The final set of tasks were setting up the boundary conditions. It is important to note that before the meshing is transferred to Fluent, that named selections of the boundary conditions should be created. This process, diagrams, and ex-

act values have been provided in the Fluent settings section of the Appendix. There were five boundary conditions that were defined: inlet, outlet, pressure far-field, axis, and nose cone profile (wall). The inlet was set to inlet velocity defined in m/s and travelled positively on the x-axis. The turbulence settings for the inlet were set to simulate those of a wind tunnel. The outlet was set as a pressure outlet and its gauge pressure of zero was set related to the atmospheric operating pressure of 101325 Pa.

The pressure far-field represented the freestream velocity and was inputted as a Mach number as opposed to a velocity. As the computational domain had been cut in half, the axis represented the line of symmetry. Finally, the nose cone profile was represented as a cut out in the computational domain, and the outline was defined as a wall. Additionally, setup for the wall was also required in the references section as the length and cross-sectional area of the nose cone were required to be inputted. The diagram below displays the computational domain as well as the boundary conditions.

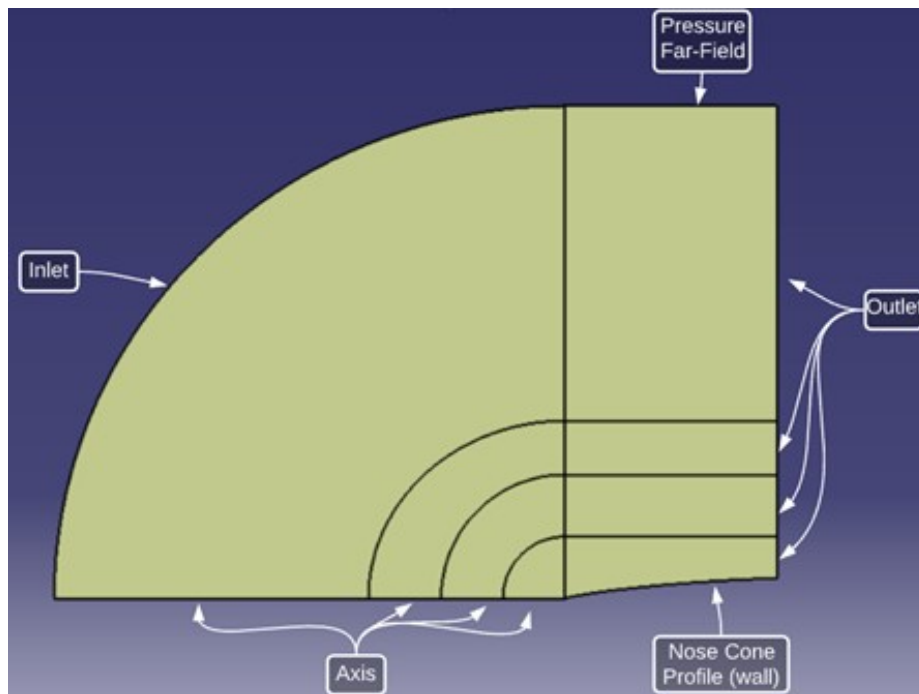


Figure 4.6: Boundary Conditions.

## 5 Validation

This section looks at validating the data acquired from the simulations. While it is very important to validate data through experimental means, due to the pandemic this was not possible. Therefore, validation was attempted through other means such as: two comparison tests,  $Y^+$  values, flow development, and a mesh independence study using the grid convergence index.

### 5.1 Comparison Tests

There were two comparison tests done to help ensure that the results collected were credible for use in the decision making for the nose cone optimization. The first comparison test was done with the study conducted by Lucas Carvalho and Geovanio Filho. Since the study contained the setup information and geometric dimensions for the conic nose cone profile, a validation simulation was created. Once the domain, mesh and setup had been created a few test cases were completed. Once the drag values from these simulations were plotted, they were consistent with the data provided in the study. Additionally, when the computational domain was changed, the cases were rerun at a test velocity of 150m/s to ensure the results were still the same. This test case helped to validate the computational domain as well as the overall fluent setup. The figure below shows the computational domain of the validation case.



Figure 5.1: Validation Case Computational Domain.

The second comparison study was done with results from a NACA report 1386. The report investigated the drag of nose cones profiles with a fineness ratio of 3 for Mach 1.24-7.4. The report contained experimental data for the Von Karman nose cone within, collected through wind tunnel testing. Using the same computational domain and settings which were validated in the first comparison test, a Von Karman nose cone with a fineness ratio of 3 was run through Mach 0.3-Mach 3. The coefficient of drag acquired through these simulations were plotted and compared against the NACA report's plots. Overall, the plots

showed good agreement between the two. There were differences however these could be explained through differences in setup as not all conditions were reported. However even with these possible sources of error the values are still within magnitude to the experimental results and theoretical results calculated in the report.

## 5.2 $Y^+$ Values

Following the comparison studies another metric was checked: the  $y^+$  values. The  $y^+$  value is a dimensionless quantity; it is the distance from the wall measured in terms of viscous lengths. In the case of nose cone, it is important for the mesh to be able to capture the viscous effects of the flow. According to the Spalart-Allmaras model, it is recommended that the  $y^+$  values should be near 1. The image below displays a plot of the  $y^+$  values for a Von Karman nose cone. A value of 1 for  $y^+$  was difficult to achieve at higher Mach numbers due to restrictions in processing power.

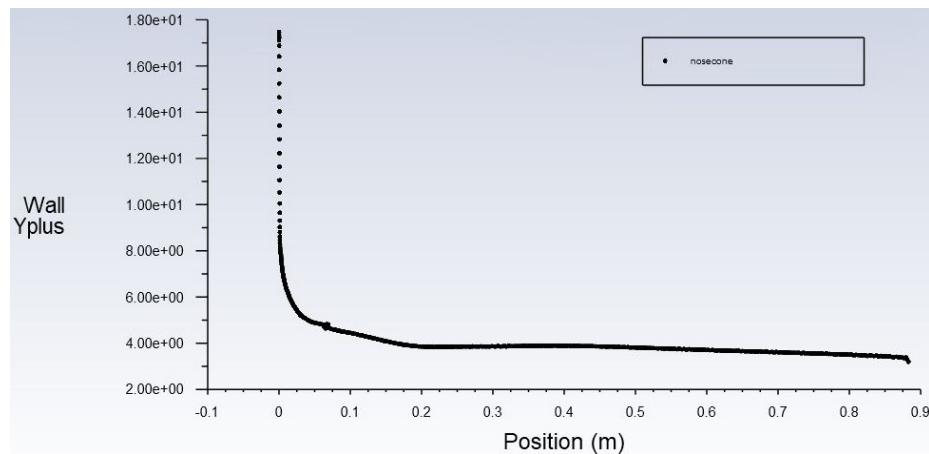


Figure 5.2:  $y^+$  Plot for FR 7 at Mach 2.5.

## 5.3 Mesh Independence Study

Once the results had been calculated from the simulations it was extremely important to check whether these results were mesh independent. In order to check this the grid convergence index was calculated. The course and fine GCIs were calculated for three Mach speeds from each region: Mach 0.5, Mach 1.5, and Mach 3. The critical variable for the grid convergence index was chosen to be the drag coefficient. To start the process the grid size of the mesh is calculated first. The grid size of a 2D domain is determined by dividing the area of the domain by the number of elements and then determining its square

root. In total three meshes were created and their respective element counts, node counts, and grid sizes can be found in table 6.

Table 4: Mesh Statistics

|        |                |                       |
|--------|----------------|-----------------------|
| Mesh 1 | O <sub>3</sub> | 13,625                |
|        | N <sub>3</sub> | 30,531                |
|        | h <sub>3</sub> | $1.06 \times 10^{-4}$ |
| Mesh 2 | O <sub>2</sub> | 216,741               |
|        | N <sub>2</sub> | 71,954                |
|        | h <sub>2</sub> | $4.48 \times 10^{-5}$ |
| Mesh 3 | O <sub>1</sub> | 691,223               |
|        | N <sub>1</sub> | 229,860               |
|        | h <sub>1</sub> | $1.90 \times 10^{-5}$ |

Once the grid size has been calculated, the next step is to calculate the grid refinement factor. It is calculated by dividing the course grid size by the fine grid size. Usually, it is desirable for the grid refinement factor to be above 1.3. In this study a grid refinement factor of 2.36 was chosen.

Table 5: Critical Variables.

| Variables        | M = 0.5  | M = 1.5 | M = 3    |
|------------------|----------|---------|----------|
| C <sub>d,3</sub> | 0.05073  | 0.12735 | 0.10505  |
| C <sub>d,2</sub> | 0.05198  | 0.12639 | 0.10756  |
| C <sub>d,1</sub> | 0.05238  | 0.12597 | 0.10891  |
| ϵ <sub>32</sub>  | -0.00125 | 0.00097 | -0.00251 |
| ϵ <sub>21</sub>  | -0.00040 | 0.00041 | -0.00135 |

The next step was to calculate the apparent order represented of the method. Since the grid refinement ratio was kept consistent for all three meshes the q(p) is zero. The table below contains the apparent order for each Mach number and includes the extrapolated Cd values as well.

Table 6: Apparent Order and Extrapolated C<sub>d</sub> Values.

| Variables                        | M = 0.5 | M = 1.5 | M = 3 |
|----------------------------------|---------|---------|-------|
| p                                | 1.325   | 0.993   | 0.727 |
| q(p)                             | 0       | 0       | 0     |
| C <sub>d,ext</sub> <sup>32</sup> | 0.053   | 0.126   | 0.110 |
| C <sub>d,ext</sub> <sup>21</sup> | 0.053   | 0.126   | 0.110 |

Next the approximate relative error was calculated at each Mach number. As seen in table 7 the approximate relative error is quite low. In both subsonic region at Mach 0.5 and supersonic region, Mach 3, the error in the first mesh was

relatively high as compared to Mach 1.5. However, with additional refinement the error dropped by 1% in both cases if not more.

Table 7: Approximate Relative Error.

| <b>Variables</b> | <b>M = 0.5</b> | <b>M = 1.5</b> | <b>M = 3</b> |
|------------------|----------------|----------------|--------------|
| $e_a^{32}$       | 2.403%         | 0.764%         | 2.334%       |
| $e_a^{21}$       | 0.766%         | 0.327%         | 1.236%       |

The extrapolated relative error was also similarly low with Mach 3 being relatively higher as compared to the other Mach numbers. This difference here can be explained by the increase in mesh density and the  $y+$  values decreasing, thus values near the end of the velocity profile were more sensitive to change.

Table 8: Extrapolated Relative Error.

| <b>Variables</b> | <b>M = 0.5</b> | <b>M = 1.5</b> | <b>M = 3</b> |
|------------------|----------------|----------------|--------------|
| $e_{ext}^{32}$   | 1.124%         | 0.573%         | 2.628%       |
| $e_{ext}^{21}$   | 0.361%         | 0.244%         | 1.409%       |

Finally, table 9 shows both the course and fine grid convergence index for all three Mach numbers. The values for all Mach numbers were low which shows that the results were not too affected by changes in Mesh. As mentioned above the velocities near Mach 3 were more sensitive to mesh changes since the boundary layer thickness decreases as velocity and therefore the Reynolds number increases.

Table 9: Fine and Course Grid Convergence Index.

| <b>Variables</b>    | <b>M = 0.5</b> | <b>M = 1.5</b> | <b>M = 3</b> |
|---------------------|----------------|----------------|--------------|
| $GCI_{course}^{32}$ | 1.421%         | 0.712%         | 3.374%       |
| $GCI_{fine}^{21}$   | 0.453%         | 0.305%         | 1.786%       |

## 6 Analysis

With the all the parameters, setup, and validation completed in previous sections, this section will analyse the data collected through the simulations. The idea here was to examine which fineness ratio proves to be the best given the criteria described in section 3.2. This section will also discuss the next steps that can be taken to further improve on this design as well as others similar in nature. Below figure 6.1 plots out all Von Karman nose cone profiles tested.

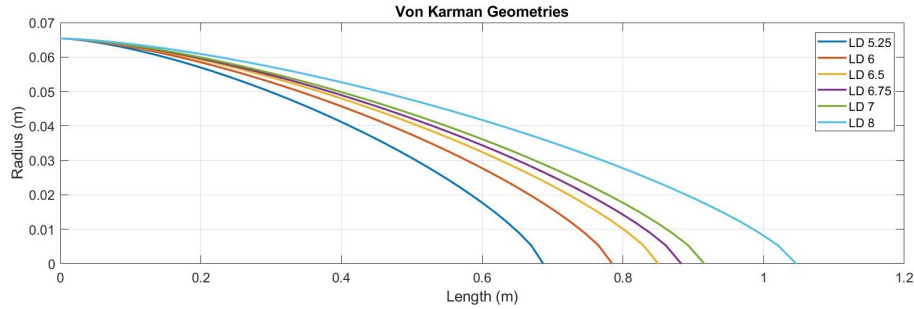


Figure 6.1: All Tested Von Karman Geometries.

### 6.1 Observations

The two main data sets collected were the drag coefficient and drag force for a set of Mach numbers, and for each fineness ratio tested. As stated in section 3.4, The process was to chose a few fineness ratios and run simulations to collect the data sets. Starting from the initial ratio of 5.25, additional ratios of 6,7, and 8 were chosen. As seen in figure 6.2 below, specifically within the supersonic region there is a large drop in the  $C_d$  between FR 5.25 and FR 6. In the supersonic region the average reduction in  $C_d$  between FR 5.25 and FR 6 was 0.0031. When comparing FR 7 and FR 6 the reduction was less than half of that between FR 5.25 and 6 and averaged out at 0.0012. Finally, when compared between FR 8 and FR 7 the change was near negligible, as shown in figure 6.2, FR 7 had a lower  $C_d$  for most of the supersonic region with the average difference being around 0.0010. Then at Mach 2.5 FR 8 intersected FR 7 and had a lower  $C_d$  then FR 7 by around 0.0007 for the rest of the Mach speeds.

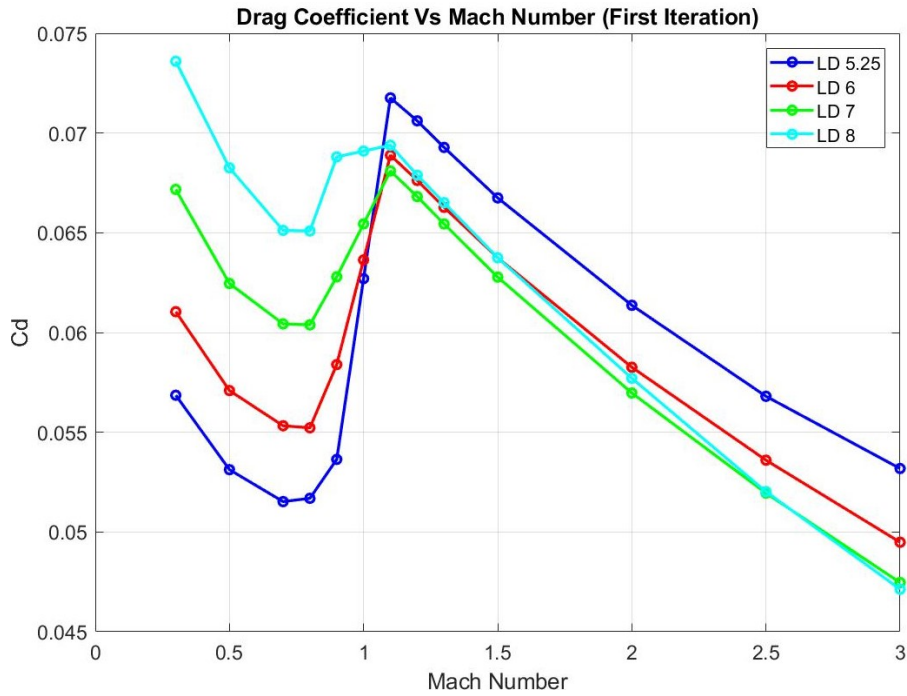


Figure 6.2: Coefficient of Drag Vs Mach Number First Iteration.

In the subsonic region however it was the opposite. With each increase in the fineness ratio the subsonic drag coefficients increased up to a maximum of 0.0041. While penalties taken in the subsonic region seem to be larger than the savings in the supersonic region, figure 6.3 which plots the drag values for each fineness ratio against the Mach numbers, shows that these penalties were negligible. As shown in figure 6.3 while there were large changes in the  $C_d$  values the actual drag incurred due to them was around 1-5N at most. Whereas the drop's in  $C_d$  within the supersonic region helped to save up to 50N as compared to the initial design.

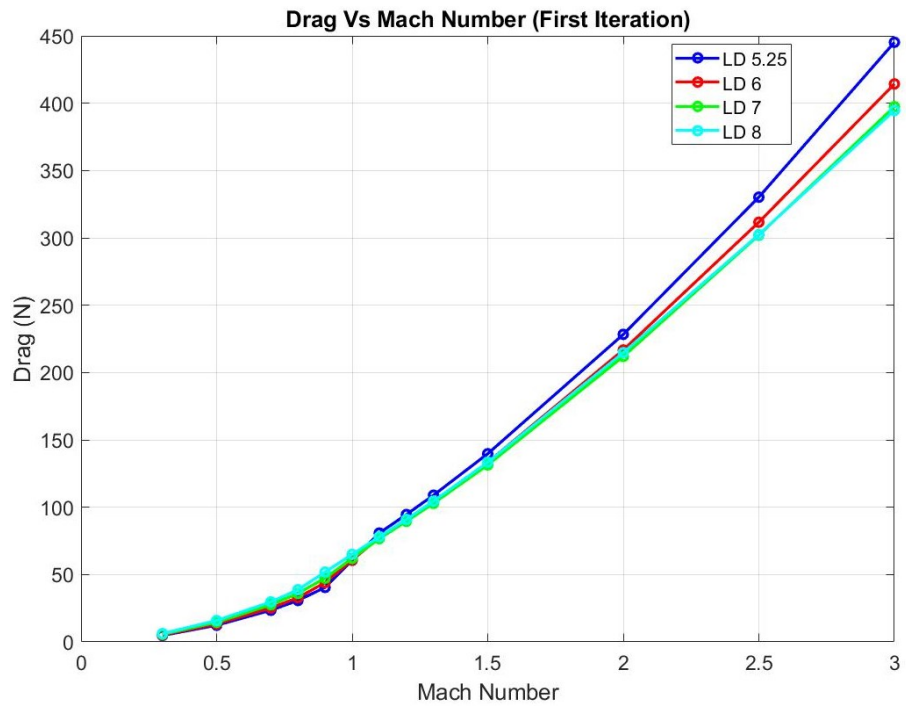


Figure 6.3: Drag Vs Mach Number First Iteration.

Therefore, based on the data in figure 6.2 the upper limit to the fineness ratio was set to be FR 7. The next fineness ratio was chosen to be 6.5 based on the bisection method. As seen in the figures 6.4 and 6.5 below at Mach 1.1 the  $C_d$  data of FR 6.5 follows FR 7 very closely, however it divergences at Mach 1.5. The values are very close as seen above even small variations in the  $C_d$  can yield major differences in the drag forces.

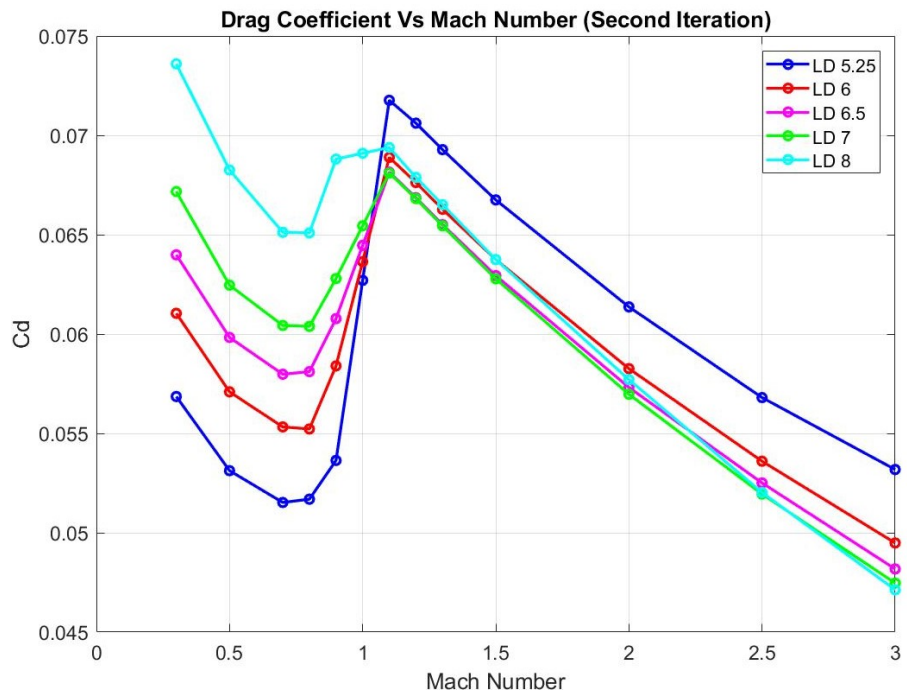


Figure 6.4: Drag Coefficient Vs Mach Number Second Iteration.

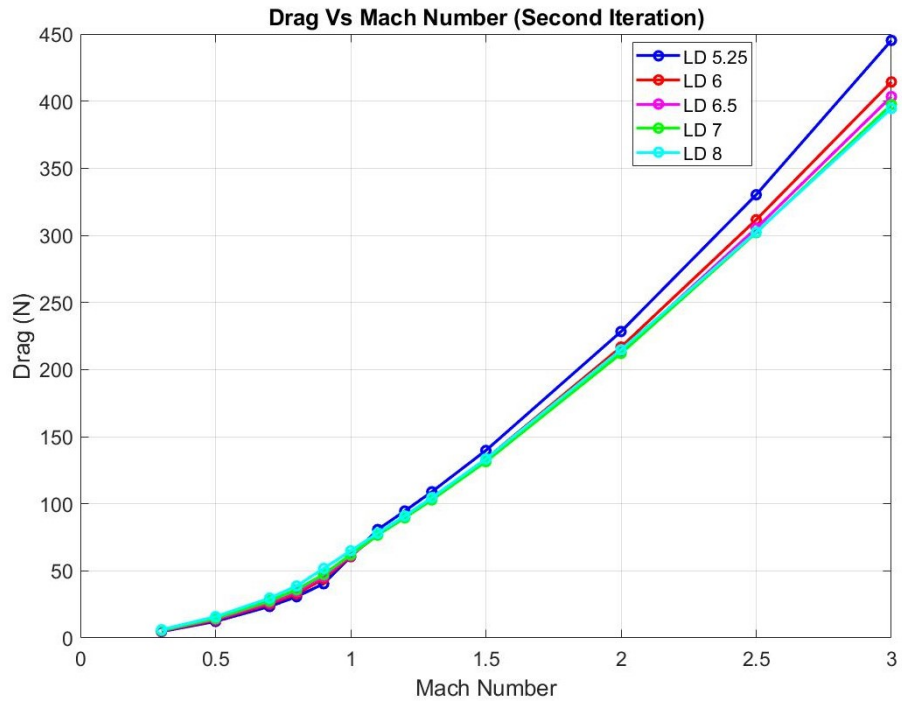


Figure 6.5: Drag Vs Mach Number Second Iteration.

The next FR was chosen to be between FR 6.5 and FR 7 at 6.75. Figures 6.6 and 6.7 display the drag coefficient and drag force data for the FR 6.75. Specifically looking at the figure 6.6 the  $C_d$  data for FR 6.75 lines up with the data for FR 7 for almost the entirety of the supersonic region. The data only starts to split from FR 7 at Mach 2.5, even after the split the data follows closely with FR 7. The drag data shown in figure 6.7 displays the same pattern. The FR of 6.75 was the last ratio on which simulations were conducted, as the data showed that it had essentially matched the limit.

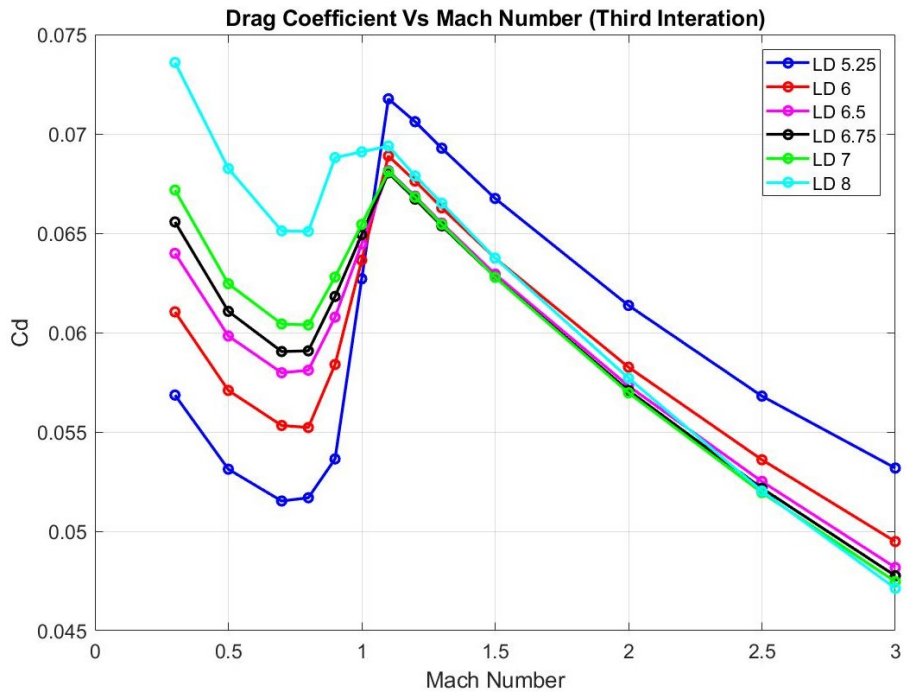


Figure 6.6: Drag Coefficient Vs Mach Number Third Iteration.

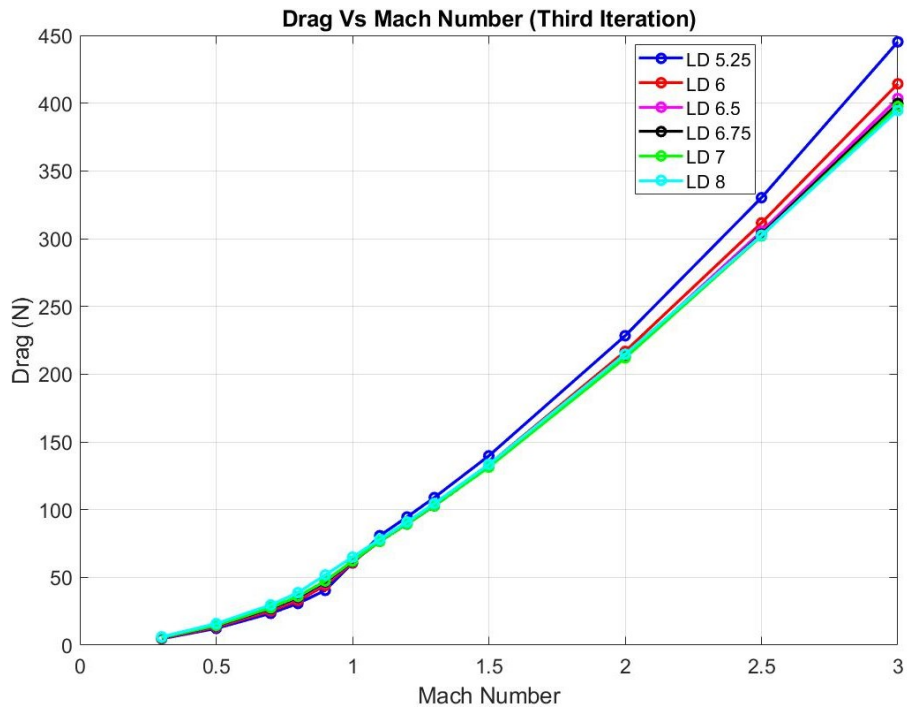


Figure 6.7: Drag Vs Mach Number Third Iteration.

In figure 6.8 below a drag coefficient breakdown has been provided. The total drag is split into three components, the first two components are: foredrag (also known as body pressure drag), and skin friction drag. The third component is the base drag, which is described as the drag generated in an object moving through a fluid from the shape of its rear end. Together they make up the total  $C_d$  values provided by Fluent. In this case base drag is not present as the computational domain was cut off at the end of the nose cone profile to simulate it being connected to the rocket body. As seen in the figure much of the total  $C_d$  can be attributed to the pressure drag, while the skin friction drag was relatively minor. The skin friction coefficient also followed the pattern of decreasing as the Mach number increased.

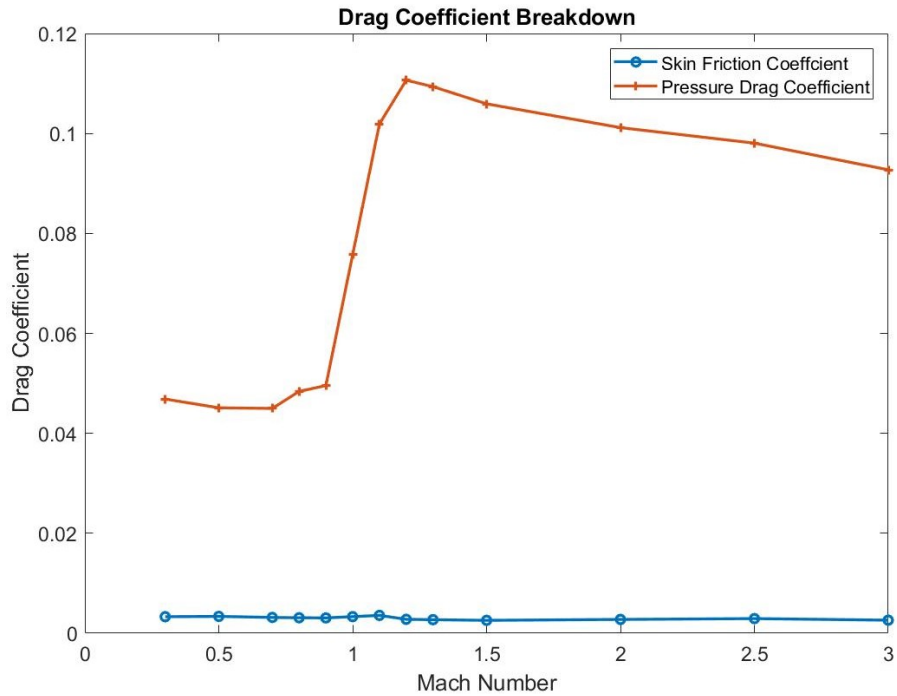


Figure 6.8: Drag Breakdown.

## 6.2 Optimized Nose Cone Selection

The selection process for the optimal nose cone is dependant on the criteria set out in section 3.5. The most important criterion was drag, followed by mass, then thermal properties and finally structural integrity. The majority of the selection was based on the supersonic region. This was due to changes in the subsonic region, even with high variations in the  $C_d$ , resulted in drag values only changing by roughly 1-2 N between fineness ratios. In figures 6.9 and 6.10 the  $C_d$  values were plotted against the fineness ratios, with each line representing a specific Mach number. In figure 6.6 and 6.9 it is evident that both FR 5.25 and FR 6 are disqualified form selection based on all other fineness ratios beating them in terms of drag in the supersonic region.

This now leaves 4 other fineness ratios: 6.5,6.75,7,8. The FR of 8 can also be disqualified on the basis that the other three FR have lower drag values than it for the entirety of the supersonic region, except for Mach 2.5 and above. The FR of 8 represents a turning point where due to its large surface area, skin friction forces are starting to become dominant. The  $C_d$  values for FR 8 trail above the values for ratios 6.5, 6.75, and 7 until Mach 2.5. Even then the values closely resemble FR 7 until the end at Mach where they only cause a roughly 3N drop in drag. The FR 6.5 is next to be disqualified. While the data for the ratio is closer to the limit established by FR 7 it is outmatched by FR 6.75 whose data

is a much closer match.

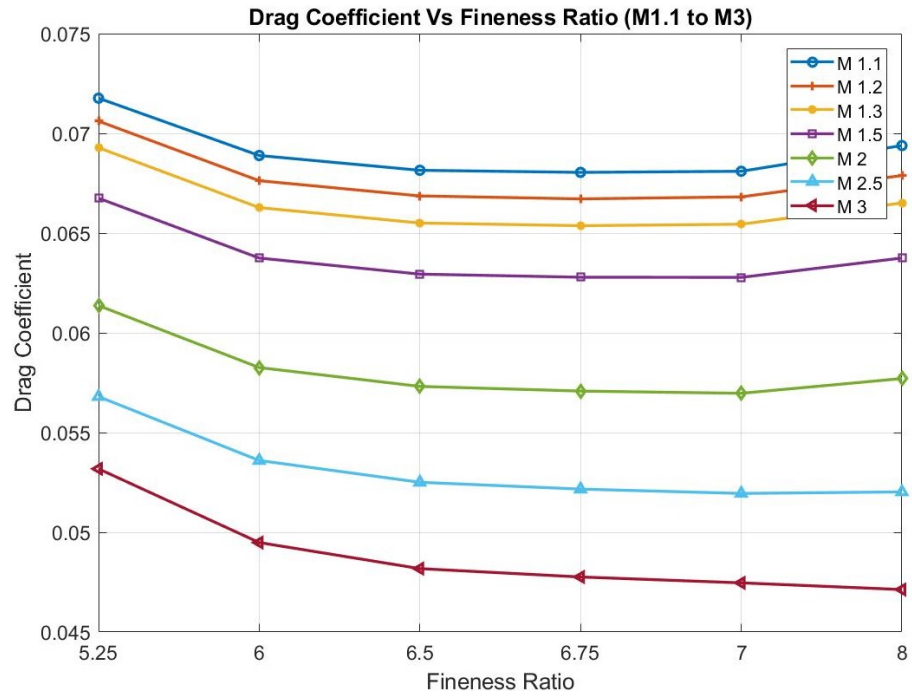


Figure 6.9: Drag Coefficient Vs Fineness Ratio (Mach 1.1 - Mach 3).

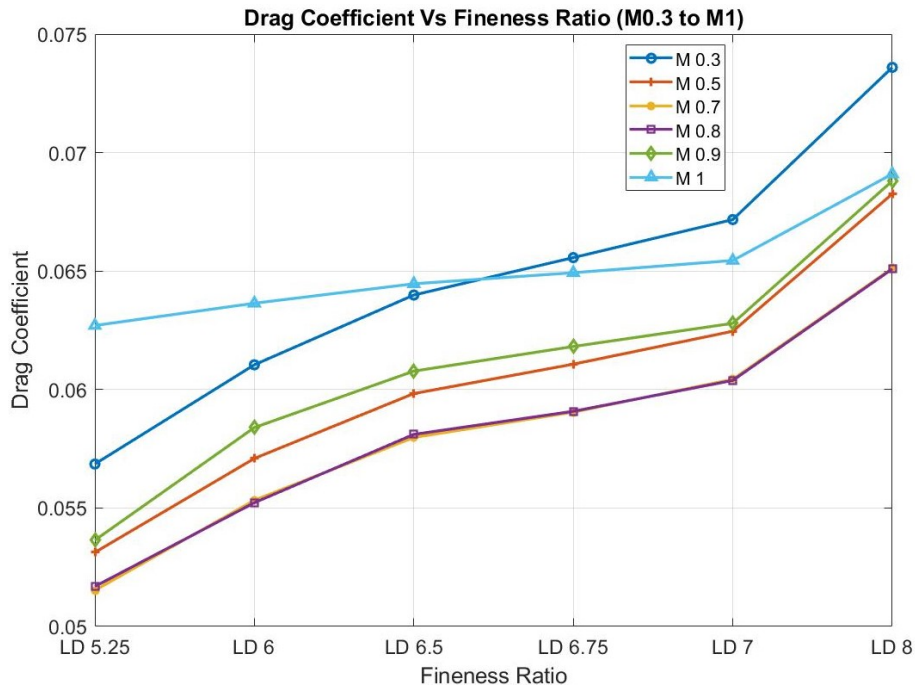


Figure 6.10: Drag Coefficient Vs Fineness Ratio (Mach 0.3 - Mach 1).

With four of the six fineness ratios disqualified this just leaves FR 6.75 and FR 7. In figure 6.9 out of the seven Mach numbers plotted, FR 6.75 had lower  $C_d$  values for Mach 1.1, 1.2, and 1.3. In the cases of Mach 2 and Mach 1.5 the difference between FR 6.75 and 7 were negligible with both ratios having near same  $C_d$  values. This trend was also mirrored in figure 6.11 which plotted the drag values vs the fineness ratios, with each line representing a specific Mach number. The figure showed that even with the slightly better performance of FR 7 over FR 6.75 at Mach 2.5 and 3, the difference in drag values was around 1-2N.

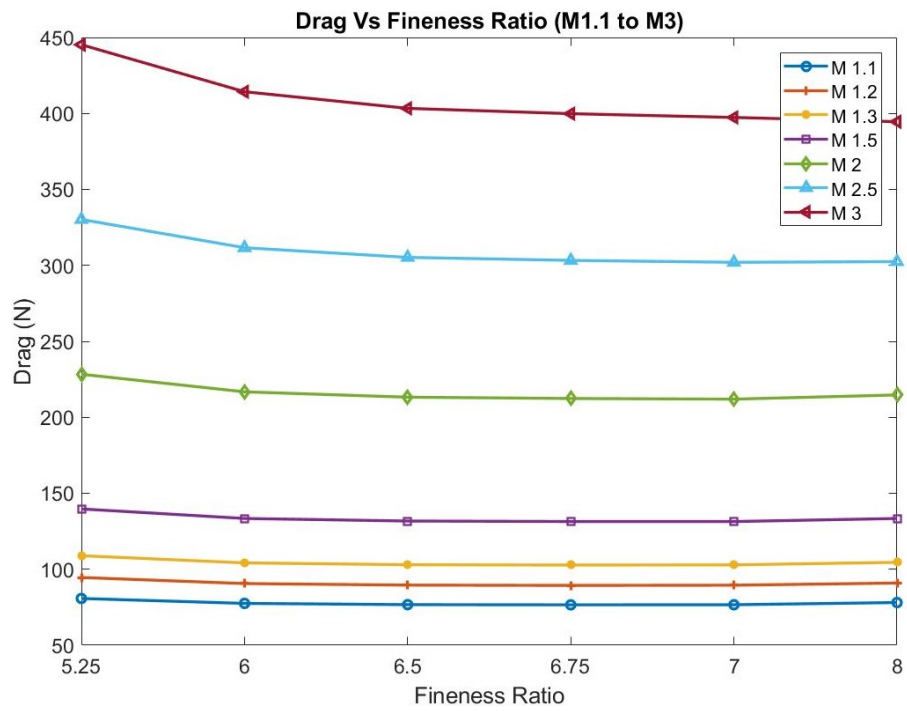


Figure 6.11: Drag Vs Fineness Ratio (Mach 1.1 - Mach 3).

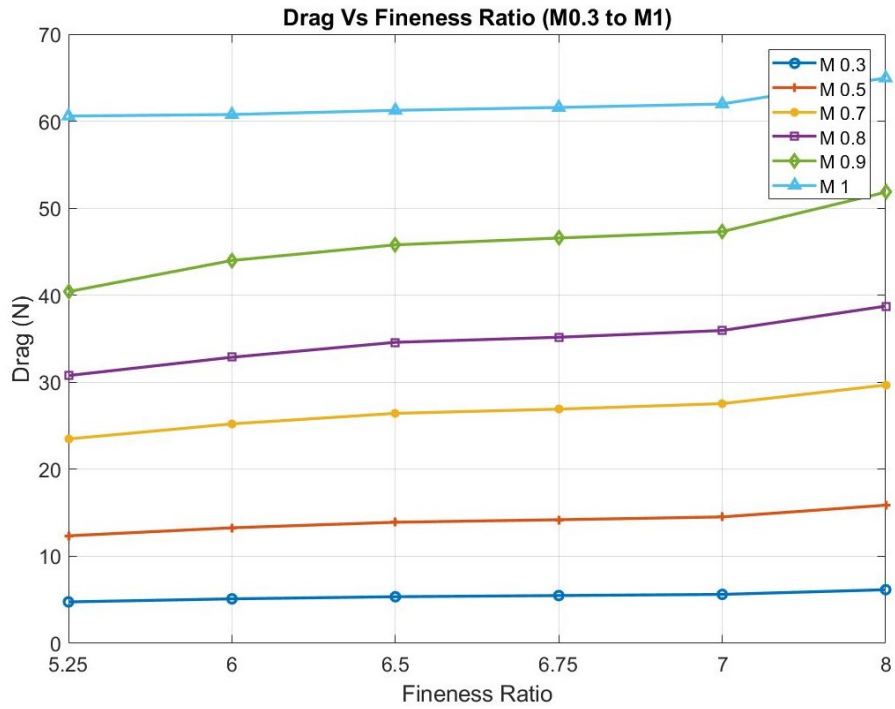


Figure 6.12: Drag Vs Fineness Ratio (Mach 0.3 - Mach 1).

Overall, it can be determined that the two FR are extremely close in terms of performance. Therefore, in order to find the optimal design between them the rest of the criterion can be utilized. The next important criterion was mass. In table 10 a few of the properties such as length, volume, mass, and cost were summarized for all fineness ratios. The table below assumes that the entire nose cone is manufactured using carbon fiber, which has a density of 1600 kg/m<sup>3</sup> and costs \$21.6/kg. Specifically focusing on fineness ratios 6.75 and 7, FR 6.75 is lighter than FR 7 by 20 grams. This weight does not include the additional mass of resin and assumes zero waste material. However once again the two ratios are close in terms of performance, therefore the last two criterions will be used to find the optimal design.

Table 10: Mass Criterion.

| Fineness Ratio | Length (m) | Volume (m <sup>3</sup> ) | Mass (kg) | Cost (\$) |
|----------------|------------|--------------------------|-----------|-----------|
| 5.25           | 0.69       | 0.000287                 | 0.46      | 9.88      |
| 6              | 0.78       | 0.000328                 | 0.52      | 11.28     |
| 6.5            | 0.85       | 0.000355                 | 0.57      | 12.22     |
| 6.75           | 0.88       | 0.000369                 | 0.59      | 12.69     |
| 7              | 0.92       | 0.000382                 | 0.61      | 13.16     |
| 8              | 1.05       | 0.000437                 | 0.70      | 15.03     |

The final two criterion are thermal properties and structural integrity. With the Von Karman nose cone geometry being a subset of ogive nose cones, it already has better thermal properties and structural integrity due to their blunted nose. In figure C.3 below this is evident as both ratios have near identical static temperatures behind the shockwaves at the apex of the nose cones with 6.75 being better.

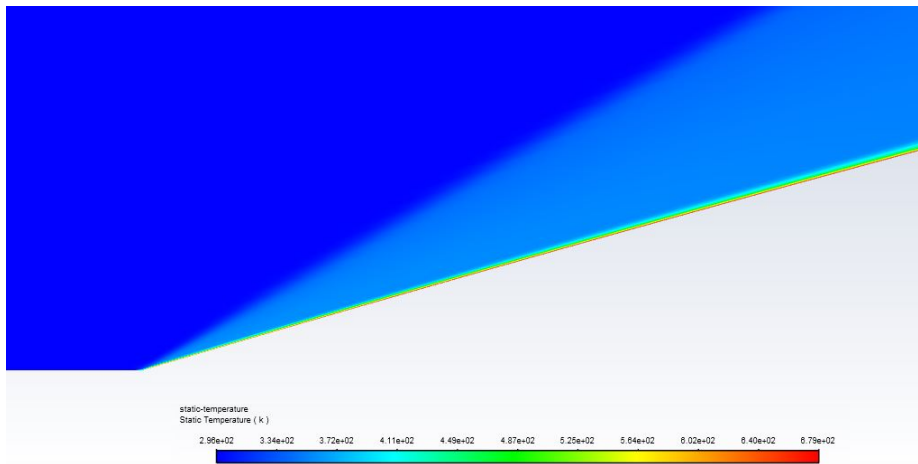


Figure 6.13: Static Temperature at Mach 2.5.

In terms of structural integrity however FR 6.75 beats FR 7, due to buckling resistance. Since the rocket, specifically the nose cone will be taking the brunt of the axial loadings, it is extremely important that the design be resistant to buckling. According to Euler's formula for buckling represented by equation 6.1, the smaller the length of the cylinder the more resistant it is to buckling. With FR 6.75 being 4 cm smaller than FR 7 it has the advantage of being a more structurally resilient design. Therefore, with all criteria being considered FR 6.75 is chosen as the optimal fineness ratio for the Von Karman nose cone geometry.

$$P_{cr} = \frac{\pi^2 EI}{L^2} \quad (6.1)$$

### 6.3 Next Steps

The next steps for this design process can be divided into a few areas of improvement. With limitations in time and computational resources further reduced, the mesh could be further refined to reduce any numerical inaccuracies. In terms of geometries, additional nose cone profiles such as the  $\frac{3}{4}$  parabola and others could be analysed in conjunction with the Von Karman profile to further research an optimized design. If possible experimental testing of the nose cone profiles could be completed through wind tunnel testing.

## 7 Conclusion

In conclusion, nose cone geometry was designed based on the conditions of the rockets flight path. The design was optimized based on preliminary measurements, aerodynamic factors, and engineering design process for the given flight profile. This analysis was done utilizing ANSYS Fluent to conduct CFD on various 2D axisymmetric Von Karman nose cone profiles of varying fineness ratios. Based on the criteria of minimum drag, mass, thermal properties, and structural integrity, the fineness ratio of 6.75 was chosen as the optimal design. The setup and the data itself were validated through a variety of methods such as: comparison to literature review, experimental data, as well as a grid convergence index analysis. The  $C_d$  values of the comparison were well within the range of experimental values, with the difference being attributed to the unknowns in setup conditions.

## 8 References

1. L. de A. S. Carvalho and G. Claudino, “CFD analysis of drag force for different nose cone design,” Research Gate, Oct. 2019.
2. S. S. Chin, Missile configuration design. 1961.
3. G. A. Crowell, “THE DESCRIPTIVE GEOMETRY OF NOSE CONES.”.
4. A. M. Drozario and S. M., “Study on Various Types of Nose Cone Profiles at Supersonic Speed through Analytical, Experimental and Numerical Simulation Methods,” Dec. 2020.
5. G. Kumar, “CFD Analysis of Transonic Flow over the Nose Cone of Aerial Vehicle,” Sep. 2015.
6. A. Narayan, N. Subramanian, and R. Kumar, “Hypersonic flow past nose cones of different geometries: a comparative study,” Oct. 2017.

## A Results.m

```
1 clear;
2 clc;
3 % results data
4 res = xlsread('D:\Uni\Fourth Year\Undergraduate ...
    Thesis\Results.xlsx', 'Comparison', 'B3:N15');
5 % mach number
6 M = res(:,1);
7 % drag coefficients
8 cd_5_25 = res(:,2);
9 cd_6 = res(:,4);
10 cd_6_5 = res(:,6);
11 cd_6_75 = res(:,8);
12 cd_7 = res(:,10);
13 cd_8 = res(:,12);
14 % drag values
15 d_5_25 = res(:,3);
16 d_6 = res(:,5);
17 d_6_5 = res(:,7);
18 d_6_75 = res(:,9);
19 d_7 = res(:,11);
20 d_8 = res(:,13);
21 % Fineness Ratio
22 ld = [1,2,3,4,5,6];
23 dm = [cd_5_25,cd_6,cd_6_5,cd_6_75,cd_7,cd_8]';
24 dd = [d_5_25,d_6,d_6_5,d_6_75,d_7,d_8]';
25 % skin friction drag and pressure drag
26 cf = xlsread('D:\Uni\Fourth Year\Undergraduate ...
    Thesis\Results.xlsx', 'LD 3', 'F4:F16');
27 pd = xlsread('D:\Uni\Fourth Year\Undergraduate ...
    Thesis\Results.xlsx', 'LD 3', 'G4:G16');
28 % plot 1 (5.25,6,7,8)
29 figure
30 plot(M,cd_5_25,'b-o',M,cd_6,'r-o',M,cd_7,'g-o',...
31     M,cd_8,'c-o','LineWidth',2)
32 title('Drag Coefficient Vs Mach Number (First ...
    Iteration)','FontSize',16)
33 xlabel('Mach Number','FontSize',16)
34 ylabel('Cd','FontSize',16)
35 legend('LD 5.25','LD 6','LD 7','LD 8')
36 set(gca,'FontSize',14)
37 grid on
38 % plot 2 (5.25,6,6.5,7,8)
39 figure
40 plot(M,cd_5_25,'b-o',M,cd_6,'r-o',M,cd_6_5,...
41     'm-o',M,cd_7,'g-o',M,cd_8,'c-o','LineWidth',2)
42 title('Drag Coefficient Vs Mach Number (Second ...
    Iteration)','FontSize',16)
43 xlabel('Mach Number','FontSize',16)
44 ylabel('Cd','FontSize',16)
45 legend('LD 5.25','LD 6','LD 6.5','LD 7','LD 8')
46 set(gca,'FontSize',14)
47 grid on
48 % plot 3 (5.25,6,6.5,6.75,7,8)
```

```

49 figure
50 plot(M,cd_5_25,'b-o',M,cd_6,'r-o',M,cd_6_5,...
51      'm-o',M,cd_6_75,'k-o',M,cd_7,'g-o',M,cd_8,...
52      'c-o','LineWidth',2)
53 title('Drag Coefficient Vs Mach Number (Third ...
      Iteration)','FontSize',16)
54 xlabel('Mach Number','FontSize',16)
55 ylabel('Cd','FontSize',16)
56 legend('LD 5.25','LD 6','LD 6.5','LD 6.75','LD 7','LD 8')
57 set(gca,'FontSize',14)
58 grid on
59 % plot 4 (5.25,6,7,8)
60 figure
61 plot(M,d_5_25,'b-o',M,d_6,'r-o',M,d_7,'g-o',...
62      M,d_8,'c-o','LineWidth',2)
63 title('Drag Vs Mach Number (First Iteration)','FontSize',16)
64 xlabel('Mach Number','FontSize',16)
65 ylabel('Drag (N)','FontSize',16)
66 legend('LD 5.25','LD 6','LD 7','LD 8')
67 set(gca,'FontSize',14)
68 grid on
69 % plot 5 (5.25,6,6.5,7,8)
70 figure
71 plot(M,d_5_25,'b-o',M,d_6,'r-o',M,d_6_5,'m-o',...
72      M,d_7,'g-o',M,d_8,'c-o','LineWidth',2)
73 title('Drag Vs Mach Number (Second Iteration)','FontSize',16)
74 xlabel('Mach Number','FontSize',16)
75 ylabel('Drag (N)','FontSize',16)
76 legend('LD 5.25','LD 6','LD 6.5','LD 7','LD 8')
77 set(gca,'FontSize',14)
78 grid on
79 % plot 6 (5.25,6,6.5,6.75,7,8)
80 figure
81 plot(M,d_5_25,'b-o',M,d_6,'r-o',M,d_6_5,'m-o',...
82      M,d_6_75,'k-o',M,d_7,'g-o',M,d_8,'c-o',...
83      'LineWidth',2)
84 title('Drag Vs Mach Number (Third Iteration)','FontSize',16)
85 xlabel('Mach Number','FontSize',16)
86 ylabel('Drag (N)','FontSize',16)
87 legend('LD 5.25','LD 6','LD 6.5','LD 6.75','LD 7','LD 8')
88 set(gca,'FontSize',14)
89 grid on
90 % plot 7
91 figure
92 plot(ld,dm(:,1),'-o',ld,dm(:,2),'-+',ld,dm(:,3),'-*',...
93      ld,dm(:,4),'-s',ld,dm(:,5),'-d',ld,dm(:,6),'-^',...
94      'LineWidth',2)
95 title('Drag Coefficient Vs Fineness Ratio (M0.3 to ...
      M1)','FontSize',16)
96 xlabel('Fineness Ratio','FontSize',16)
97 ylabel('Drag Coefficient','FontSize',16)
98 legend('M 0.3','M 0.5','M 0.7','M 0.8','M 0.9','M 1')
99 xticks([1 2 3 4 5 6])
100 xticklabels({'LD 5.25','LD 6','LD 6.5','LD 6.75','LD 7','LD 8'})
101 set(gca,'FontSize',14)
102 grid on
103 % plot 8

```

```

104 figure
105 plot(ld, dm(:, 7), '-o', ld, dm(:, 8), '-+', ld, dm(:, 9), '-*', ...
106      ld, dm(:, 10), '-s', ld, dm(:, 11), '-d', ld, dm(:, 12), '-^', ...
107      ld, dm(:, 13), '-<', 'LineWidth', 2)
108 title('Drag Coefficient Vs Fineness Ratio (M1.1 to ...
      M3)', 'FontSize', 16)
109 xlabel('Fineness Ratio', 'FontSize', 16)
110 ylabel('Drag Coefficient', 'FontSize', 16)
111 legend('M 1.1', 'M 1.2', 'M 1.3', 'M 1.5', 'M 2', 'M 2.5', 'M 3')
112 xticks([1 2 3 4 5 6])
113 xticklabels({'5.25', '6', '6.5', '6.75', '7', '8'})
114 set(gca, 'FontSize', 14)
115 grid on
116 % plot 9
117 figure
118 plot(ld, dd(:, 1), '-o', ld, dd(:, 2), '-+', ld, dd(:, 3), '-*', ...
119      ld, dd(:, 4), '-s', ld, dd(:, 5), '-d', ld, dd(:, 6), '-^', ...
120      'LineWidth', 2)
121 title('Drag Vs Fineness Ratio (M0.3 to M1)', 'FontSize', 16)
122 xlabel('Fineness Ratio', 'FontSize', 16)
123 ylabel('Drag (N)', 'FontSize', 16)
124 legend('M 0.3', 'M 0.5', 'M 0.7', 'M 0.8', 'M 0.9', 'M 1')
125 xticks([1 2 3 4 5 6])
126 xticklabels({'5.25', '6', '6.5', '6.75', '7', '8'})
127 set(gca, 'FontSize', 14)
128 grid on
129 % plot 10
130 figure
131 plot(ld, dd(:, 7), '-o', ld, dd(:, 8), '-+', ld, dd(:, 9), '-*', ...
132      ld, dd(:, 10), '-s', ld, dd(:, 11), '-d', ld, dd(:, 12), '-^', ...
133      ld, dd(:, 13), '-<', 'LineWidth', 2)
134 title('Drag Vs Fineness Ratio (M1.1 to M3)', 'FontSize', 16)
135 xlabel('Fineness Ratio', 'FontSize', 16)
136 ylabel('Drag (N)', 'FontSize', 16)
137 legend('M 1.1', 'M 1.2', 'M 1.3', 'M 1.5', 'M 2', 'M 2.5', 'M 3')
138 xticks([1 2 3 4 5 6])
139 xticklabels({'5.25', '6', '6.5', '6.75', '7', '8'})
140 set(gca, 'FontSize', 14)
141 % plot 11
142 figure
143 plot(M, cf, '-o', M, pd, '-+', 'LineWidth', 2)
144 title('Drag Coefficient Breakdown', 'FontSize', 16)
145 xlabel('Mach Number', 'FontSize', 16)
146 ylabel('Drag Coefficient', 'FontSize', 16)
147 legend('Skin Friction Coefficient', 'Pressure Drag Coefficient')
148 set(gca, 'FontSize', 14)

```

## B Von-Karman-Profile-Coordinates.m

```
1 %% Von Karman Profile Coordinates
2 clc;
3 clear;
4 in = 25.4; %in to mm conversion
5 ld = [5.25,6,6.5,6.75,7,8]'; %user option
6 d = 5.15; %nose cone diameter
7 r = d/2; %nose cone radius
8 l = d*ld; %nose cone length
9 c = 0; %for von karman shape
10 per = linspace(0,1,41);
11 x = l*per;
12 theta = acos(1-((2.*x)./l));
13 y = r*sqrt(theta-(sin(2.*theta)/2)+(c*sin(theta).^3))/sqrt(pi)/1000;
14 X = x*in;
15 Y = y*in;
16 Z = zeros(1,length(per));
17 co = [X;Y;Z]';
18 coord = flip(co,1)/1000;
19 % a = coord(:,1)
20 % b = Y(1,:);
21
22 figure
23 plot(coord(:,1),Y(1,:))
24 title('Initial Von Karman Geometry','FontSize',16,'LineWidth',2)
25 xlabel('Length (m)','FontSize',16)
26 ylabel('Radius (m)','FontSize',16)
27 legend('LD 5.25')
28 grid on
29 set(gca,'FontSize',14)
30
31 figure
32 plot(coord(:,1),Y(1,:),coord(:,2),Y(1,:),coord(:,3),Y(1,:),...
33       coord(:,4),Y(1,:),coord(:,5),Y(1,:),coord(:,6),Y(1,:),...
34       'LineWidth',2)
35 title('Von Karman Geometries','FontSize',16)
36 xlabel('Length (m)','FontSize',16)
37 ylabel('Radius (m)','FontSize',16)
38 legend('LD 5.25','LD 6','LD 6.5','LD 6.75','LD 7','LD 8')
39 grid on
40 set(gca,'FontSize',14)
```

## C Fluent Settings

This section contains images of the exact Fluent settings to allow for easy repeatability of this study in the future

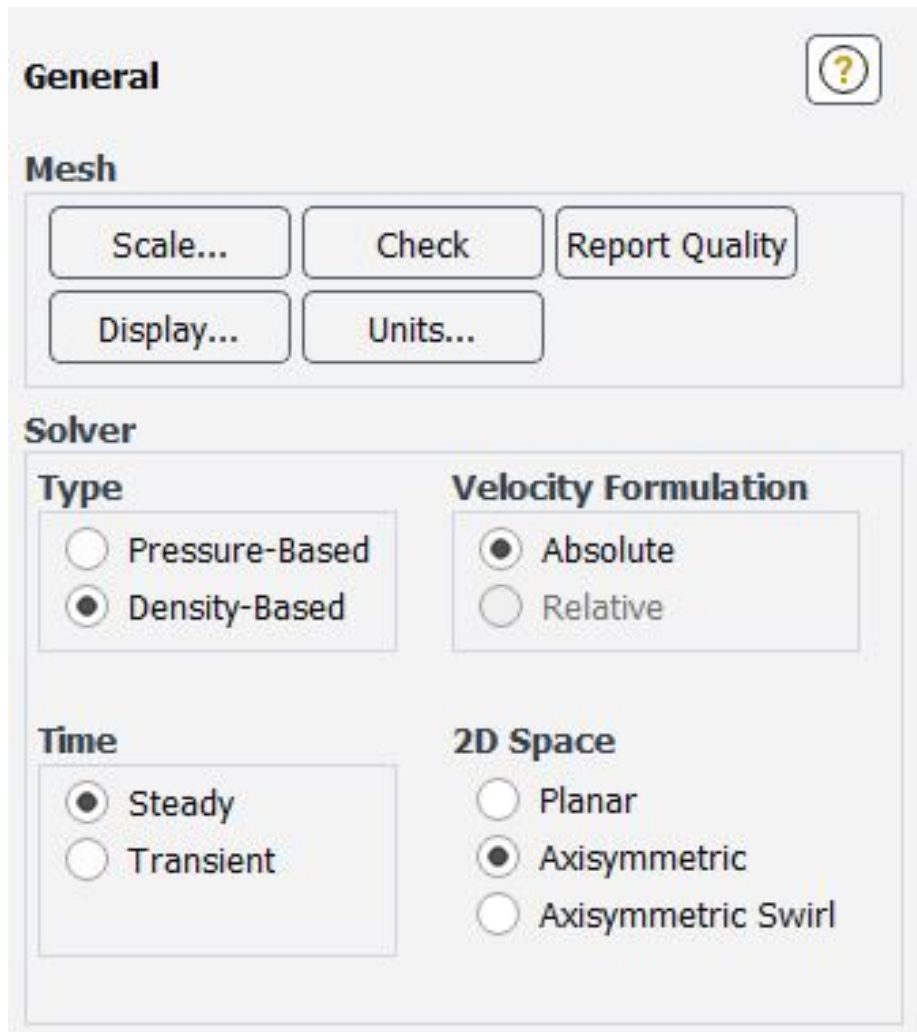


Figure C.1: Fluent General Settings.

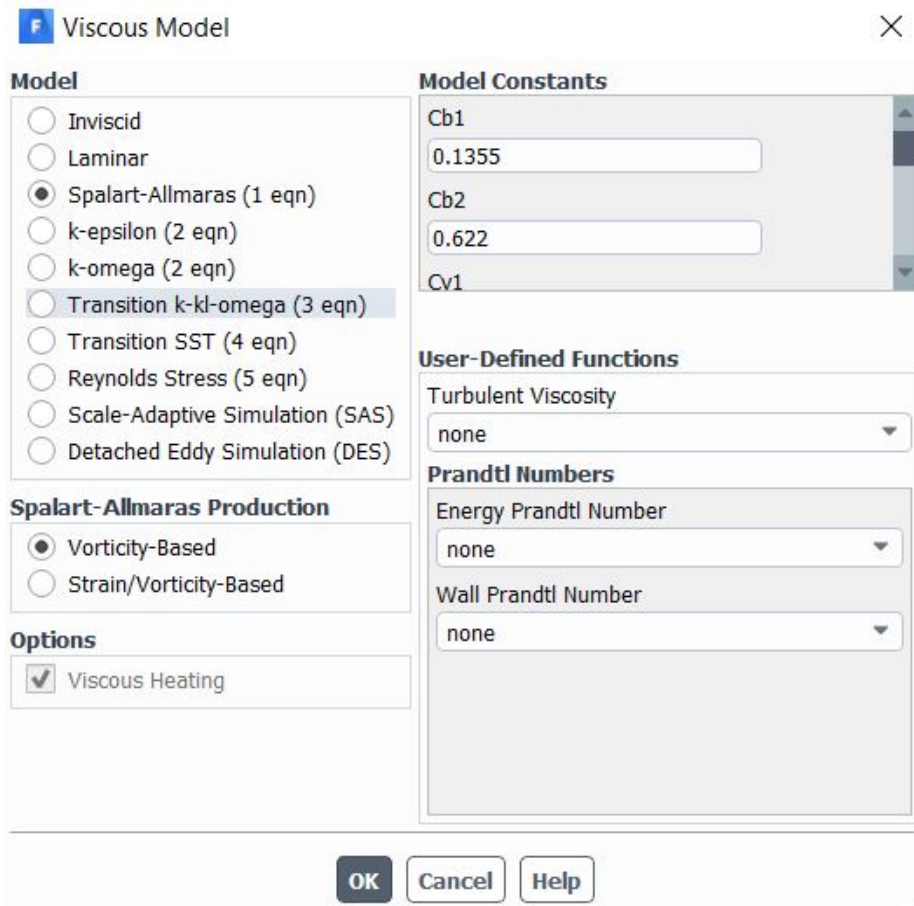


Figure C.2: Fluent Viscous Model.

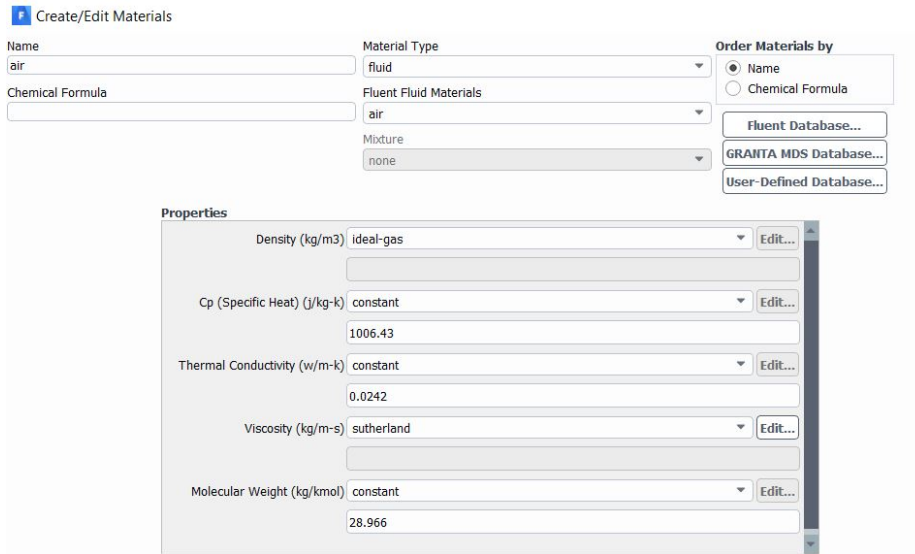


Figure C.3: Fluent Material Properties.

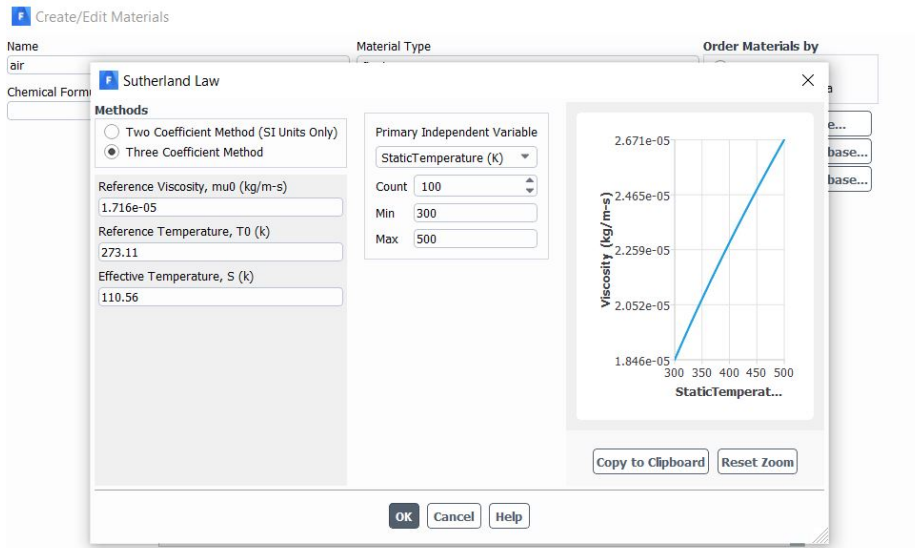


Figure C.4: Fluent Material Properties Sutherland's Law.



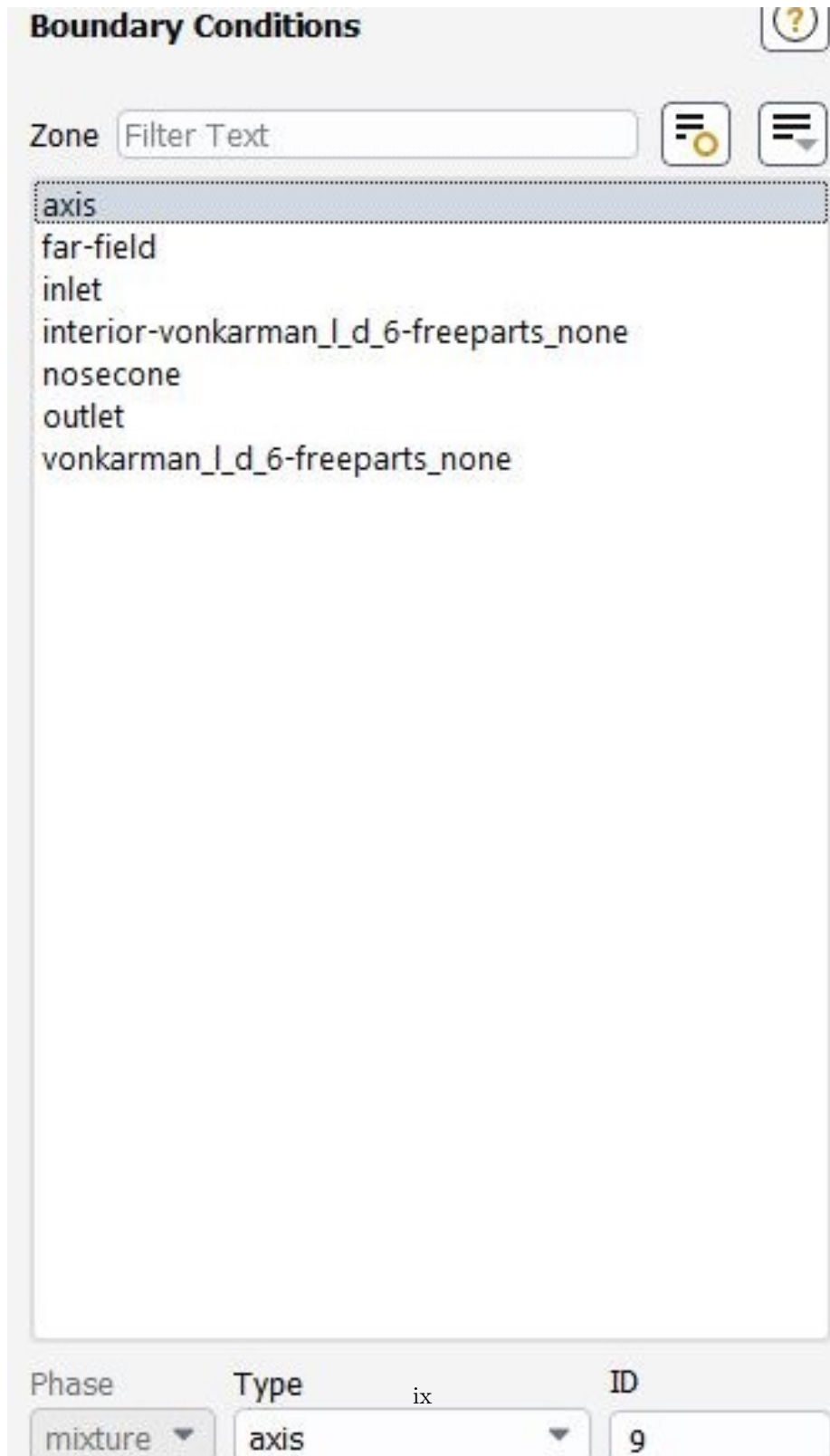


Figure C.6: Fluent Boundary Conditions.

**Reference Values** ?

Compute from

**Reference Values**

|                              |            |
|------------------------------|------------|
| Area (m <sup>2</sup> )       | 0.01343915 |
| Density (kg/m <sup>3</sup> ) | 1.176655   |
| Enthalpy (j/kg)              | 0          |
| Length (m)                   | 0.8829675  |
| Pressure (pascal)            | 0          |
| Temperature (k)              | 300        |
| Velocity (m/s)               | 857.5001   |
| Viscosity (kg/m-s)           | 1.7894e-05 |
| Ratio of Specific Heats      | 1.4        |
| Yplus for Heat Tran. Coef.   | 300        |

Reference Zone

Figure C.7: Fluent Reference Values.

**Solution Controls** 

Courant Number

**Under-Relaxation Factors**

Modified Turbulent Viscosity

Turbulent Viscosity

Solid

Figure C.8: Fluent Courant Number.

**Solution Initialization** 

**Initialization Methods**

Hybrid Initialization  
 Standard Initialization

Compute from  
inlet ▼

**Reference Frame**

Relative to Cell Zone  
 Absolute

**Initial Values**

Gauge Pressure (pascal)  
0

Axial Velocity (m/s)  
857.5001

Radial Velocity (m/s)  
0

Modified Turbulent Viscosity (m<sup>2</sup>/s)  
3.059521e-05

Temperature (k)  
300

xii

Figure C.9: Fluent Initialization.

## D Computation Domain Construction and Mesh Process

The computational domain was constructed utilizing CATIA V5 in the Generative Shape Design (GSD) toolbox. All settings for meshing and the construction of the computational domain will follow the labels provided by figure 4.2 in section 4.2. Following the dimensions that were shown in 4.1 and figure 4.1 the measurements below describe the other cuts.

1. 3 sub cuts
  - (a) Offset of curved area (1016 mm)
  - (b) 2 circles of diameter 800 mm and 400 mm

Mesh Settings for the finest mesh ( $h_1$ ), these settings can be adjusted for a finer mesh.

1. Face sizing on
  - (a) Faces 3 and 4, element size 4.5 mm
  - (b) Faces 5 and 6, element size 2.5 mm
  - (c) Faces 7 and 8, element size 1.75 mm
2. Edge sizing on edges between regions 1,3 and 2,4
  - (a) Element size 4.5 mm
3. Edge sizing on three vertical lines in the structured region (1 and 2)
  - (a) Number of divisions 75
  - (b) Bias factor 10 (towards nose cone)
4. 2 Vertex sizing on apex of nose cone
  - (a) First Sphere of influence, Sphere radius 30 mm, Element size 0.4 mm
  - (b) Second Sphere of influence, Sphere radius 10 mm, Element size 0.06 mm
5. Inflation
  - (a) Boundary is nose cone wall
  - (b) First layer thickness 0.01 mm
  - (c) 15 layers

## E GCI Calculations

Grid Size

$$h = \left[ \frac{1}{N} \sum_{i=1}^N (\Delta A_i) \right]^{1/2}$$
$$h = 1.90 \times 10^{-5}$$

### E.1 Grid Refinement Factor

$$r = h_{course} / h_{fine}$$
$$r = 4.48 \times 10^{-5} / 1.90 \times 10^{-5}$$
$$r = 2.36$$

### E.2 Critical Variables

$$\varepsilon_{32} = \phi_3 - \phi_2$$
$$\varepsilon_{32} = 0.05073 - 0.05198$$
$$\varepsilon_{32} = -0.00125$$

### E.3 Apparent Order

$$p = 1 / \ln(r_{21}) * \left| \ln \left| \frac{\varepsilon_{32}}{\varepsilon_{21}} \right| + q(p) \right|$$
$$p = 1 / \ln(2.36) * \left| \ln \left| \frac{-0.00125}{-0.00040} \right| + 0 \right|$$
$$p = 1.325$$

### E.4 Extrapolated Critical Variables

$$\phi_{ext}^{21} = \frac{(r_{21}^p \phi_1 - \phi_2)}{(r_{21}^p - 1)}$$
$$\phi_{ext}^{21} = \frac{((2.36^{1.325})(0.05238) - 0.05198)}{(2.36^{1.325} - 1)}$$
$$\phi_{ext}^{21} = 0.053$$

### E.5 Approximated Relative Error

$$e_a^{21} = \left| \frac{\phi_1 - \phi_2}{\phi_1} \right|$$
$$e_a^{21} = \left| \frac{0.05238 - 0.05198}{0.05238} \right|$$
$$e_a^{21} = 0.766\%$$

### E.6 Extrapolated Relative Error

$$e_{ext}^{21} = \left| \frac{\phi_{ext}^{12} - \phi_1}{\phi_{ext}^{21}} \right|$$
$$e_{ext}^{21} = \left| \frac{0.053 - 0.05238}{0.053} \right|$$
$$e_{ext}^{21} = 0.361\%$$

## E.7 Grid Convergence Index

$$\begin{aligned} GCI_{fine}^{21} &= \frac{1.25e_a^{21}}{r_{21}^p - 1} \\ GCI_{fine}^{21} &= \\ &= 2.36^{1.325} - 1 \\ GCI_{fine}^{21} &= 0.453\% \end{aligned}$$

## F Tabulated Results

Table A1:  $C_D$  Values for FR 5.25, 6, 6.5.

| <b>Mach Number</b> | <b>FR 5.25</b> | <b>FR 6</b> | <b>FR 6.5</b> |
|--------------------|----------------|-------------|---------------|
| 0.3                | 0.05686        | 0.06104     | 0.06399       |
| 0.5                | 0.05313        | 0.05709     | 0.05983       |
| 0.7                | 0.05152        | 0.05533     | 0.05798       |
| 0.8                | 0.05169        | 0.05522     | 0.05811       |
| 0.9                | 0.05364        | 0.05839     | 0.06078       |
| 1                  | 0.06270        | 0.06364     | 0.06446       |
| 1.1                | 0.07176        | 0.06889     | 0.06815       |
| 1.2                | 0.07061        | 0.06763     | 0.06686       |
| 1.3                | 0.06928        | 0.06628     | 0.06550       |
| 1.5                | 0.06675        | 0.06375     | 0.06294       |
| 2                  | 0.06137        | 0.05826     | 0.05731       |
| 2.5                | 0.05680        | 0.05360     | 0.05251       |
| 3                  | 0.05318        | 0.04949     | 0.04818       |

Table A2:  $C_D$  Values for FR 5.25, 6, 6.5.

| <b>Mach Number</b> | <b>FR 5.25</b> | <b>FR 6</b> | <b>FR 6.5</b> |
|--------------------|----------------|-------------|---------------|
| 0.3                | 0.06557        | 0.06717     | 0.07360       |
| 0.5                | 0.06107        | 0.06246     | 0.06826       |
| 0.7                | 0.05905        | 0.06043     | 0.06512       |
| 0.8                | 0.05908        | 0.06038     | 0.06509       |
| 0.9                | 0.06182        | 0.06279     | 0.06880       |
| 1                  | 0.06493        | 0.06545     | 0.06910       |
| 1.1                | 0.06804        | 0.06810     | 0.06939       |
| 1.2                | 0.06671        | 0.06682     | 0.06788       |
| 1.3                | 0.06537        | 0.06544     | 0.06651       |
| 1.5                | 0.06279        | 0.06278     | 0.06375       |
| 2                  | 0.05708        | 0.05697     | 0.05771       |
| 2.5                | 0.05217        | 0.05195     | 0.05203       |
| 3                  | 0.04776        | 0.04746     | 0.04713       |

Table A3: Drag Values for FR 5.25, 6, 6.5.

| <b>Mach Number</b> | <b>FR 5.25</b> | <b>FR 6</b> | <b>FR 6.5</b> |
|--------------------|----------------|-------------|---------------|
| 0.3                | 4.76           | 5.11        | 5.36          |
| 0.5                | 12.35          | 13.28       | 13.91         |
| 0.7                | 23.48          | 25.22       | 26.43         |
| 0.8                | 30.77          | 32.88       | 34.59         |
| 0.9                | 40.42          | 44.00       | 45.79         |
| 1                  | 60.59          | 60.77       | 61.25         |
| 1.1                | 80.77          | 77.54       | 76.70         |
| 1.2                | 94.59          | 90.58       | 89.56         |
| 1.3                | 108.91         | 104.19      | 102.98        |
| 1.5                | 139.70         | 133.42      | 131.73        |
| 2                  | 228.33         | 216.77      | 213.25        |
| 2.5                | 330.24         | 311.62      | 305.27        |
| 3                  | 445.23         | 414.29      | 403.34        |

Table A4: Drag Values for FR 6.75, 7, 8.

| <b>Mach Number</b> | <b>FR 5.25</b> | <b>FR 6</b> | <b>FR 6.5</b> |
|--------------------|----------------|-------------|---------------|
| 0.3                | 5.49           | 5.62        | 6.16          |
| 0.5                | 14.20          | 14.52       | 15.87         |
| 0.7                | 26.91          | 27.55       | 29.68         |
| 0.8                | 35.17          | 35.95       | 38.75         |
| 0.9                | 46.58          | 47.31       | 51.84         |
| 1                  | 61.58          | 61.98       | 64.97         |
| 1.1                | 76.59          | 76.65       | 78.10         |
| 1.2                | 89.36          | 89.50       | 90.93         |
| 1.3                | 102.77         | 102.88      | 104.56        |
| 1.5                | 131.41         | 131.39      | 133.43        |
| 2                  | 212.39         | 211.97      | 214.72        |
| 2.5                | 303.28         | 302.02      | 302.46        |
| 3                  | 399.84         | 397.37      | 394.56        |